Fracture Behavior and Simulation of X52 Steel Pipe SENT Specimens

by

Enayatallah Najari

A thesis submitted in partial fulfillment of the requirements for the degree of

Master of Science

in
Structural Engineering

Department of Civil and Environmental Engineering
University of Alberta

Abstract

Understanding the fracture behavior of pipeline steel is crucial for ensuring the integrity of pipelines in the energy transportation industry. This comprehensive thesis investigates the fracture toughness properties of API 5L AO Smith X52 pipe steel through a combination of experimental tests and numerical analysis.

The experimental component of the study utilizes Single-Edge Notched Tension (SENT) specimens to examine fracture behavior. The focus is on assessing critical parameters such as Crack Tip Opening Displacement (CTOD), Crack Mouth Opening Displacement (CMOD), and crack growth length (Δa). To achieve precise displacement measurements in small-sized samples, Digital Image Correlation (DIC) is employed. The establishment of resistance curves (R-curves) for SENT specimens is a key aspect, and the results are used to evaluate the fracture toughness properties, including Force-CTOD, Force-CMOD, CTOD-Δa, and J-Δa curves.

The findings reveal consistent fracture behavior across different crack sizes and highlight variations in fracture toughness among different steel grades. This research contributes significantly to the understanding and characterization of pipe steels.

In parallel, the numerical analysis component of the thesis the Extended Finite Element Method (XFEM) to predict crack initiation and propagation employs in SENT specimens fabricated from the same API 5L AO Smith X52 pipe steel. Specific fracture parameters, Maxpe and Gc, are used to enhance prediction accuracy. The XFEM models are rigorously compared with experimental results, focusing on Force-CTOD, Force-CMOD, and Force-Global Displacement curves. The study reaffirms the reliability of XFEM in predicting

fracture parameters across varying geometries. This research underscores the critical role of fracture mechanics in pipeline integrity assessment and contributes to advancements in fracture behavior analysis for pipeline steel materials. Future investigations are planned to expand the scope of the study by exploring other loading constraints and specimen geometries of the same steel grade.

Acknowledgements

Table of Contents

List of Tables

List of Figures

List of Symbols and Abbreviations

a	Crack length or depth of a fracture toughness test specimen
$a0$	Original crack length
A	Cross-sectional area
$A0$	Original cross-sectional area
ΔA	Reduction of cross-sectional area
b	Crack remaining ligament ($b = w - a$)
$b0$	Original crack remaining ligament ($b0 = w - a0$)
B	Thickness of a fracture toughness test specimen
w	Width of a fracture toughness test specimen
°C	Degrees Celsius
D	Outer diameter of the pipe
E	Young's modulus (Modulus of elasticity)
G	Energy release rate
GIc	Plain strain fracture toughness characterized by G
J	J- integral (a line or surface integral that encloses the crack tip from one crack surface to the other)
Jc	Value of J at fracture instability before stable tearing crack extension
J_{IC}	Plane strain fracture toughness characterized by J- integral (at the initiation of ductile cracking)
Jel	Elastic component of J ($Jel = G$)
Jpl	Plastic component of
K	Bulk Modulus
K	Stress intensity factor
K_{IC}	Plane stress fracture toughness characterized by K-factor
n	Strain hardening exponent of Hollomon equations
r	Inner radius of the pipe
t	Thickness of pipe wall
Ts	Temperature shift in Barsom & Rolfe Correlation

γ	Shear strain
δ	Crack-tip opening displacement (CTOD)
δ	CTOD at fracture instability without significant stable tearing crack extension
δIc	Plane strain fracture toughness characterized by CTOD (at the initiation of ductile cracking)
δu	Value of CTOD at fracture instability after stable tearing
εeng	Engineering strain
$\varepsilon true$	True strain
$\varepsilon t\ crit$	Longitudinal tensile strain capacity
εe	Elastic strain
εp	Plastic stain
εf	True fracture strain
εh	Hoop strain
σeng	Engineering stress
$\sigma true$	True Stress
σh	Hoop stress
σTS	Ultimate tensile strength
σYS	Yield strength
τ	Shear stress
ν	Poisson's ratio

Abbreviations

API	American Petroleum Institute
ASM	American Society for Metals
ASME	American Society of Mechanical Engineers
ASTM	American Society of Testing and Materials
BS	British Standard
CT	Compact Tension
CVN	Charpy V-notch impact energy
CSA	Canadian Standard Association
CTOD	Crack-tip opening displacement
CMOD	Crack-mouth opening displacement
DSC	Damage Stabilization Cohesive
HAZ	Heat-affected zone
HSS	High strength steel
ISO	Organization for Standardization
MTS	Material testing systems
NDT	Nondestructive testing
NPS	Nominal pipe size or diameter base on inches
SENB	Single Edge Notched Bend
SENT	Single Edge Notched Tension
SMY	Specified minimum yield strength

1. Introduction

1.1 Introduction and Background

Oil pipelines, often unseen beneath the ground surface, serve as the silent means of energy transport. These intricate systems facilitate the movement of oil from production sources to the world's energy consumers. While hidden from view, these pipelines face so many challenges, both internal and external, that threaten their reliability and integrity. Understanding and resolving the typical problems, structural stresses, and complicated dynamics of these pipelines is paramount to ensuring the safe and efficient distribution of this critical resource.

1.1.1 Specification of pipe grades

In Pipeline industry, the grade of the steel is usually represented by a letter followed by a number. For instance, X52 (L360) denotes a specific grade. The letter 'X' reveals the material's chemical composition, while the number, like 52 or 360, corresponds to the specified minimum yield strength (SMYS), either in inch-pound (ksi) or SI (MPa) units. To delve deeper into these grades and their properties, the tensile requirements for X52, X60, X65, X80, and X100 pipes are detailed in API Spec 5L [1].

1.1.2 Toughness characteristic of steel grades

Toughness, defined as the ability of a metal to deform plastically and absorb energy before fracture, underscores the importance of energy absorption in assessing a material resilience [2]. It's crucial to note that ductility, measuring the plastic deformation of a material before fracturing, doesn't solely determine toughness. A toughness hinges on a balanced interplay of strength and ductility. Materials with both high strength and ductility exhibit greater toughness compared to those with low strength and high ductility. To quantify toughness, one common method involves calculating the area under the stress-strain curve derived from a tensile test,

represented as "material toughness" in terms of energy per unit volume. Material toughness signifies the gradual energy absorption by the material [2].

In Figure 1.1 below, we can observe a comparison between the stress-strain curves of high-strength, medium-strength, and low-strength steels. Interestingly, it becomes evident that the medium-strength steel, as sourced from NDT Resource Centre, displays the most remarkable toughness. This observation underscores that achieving exceptional toughness hinges on maintaining an optimal equilibrium between high strength and significant ductility.
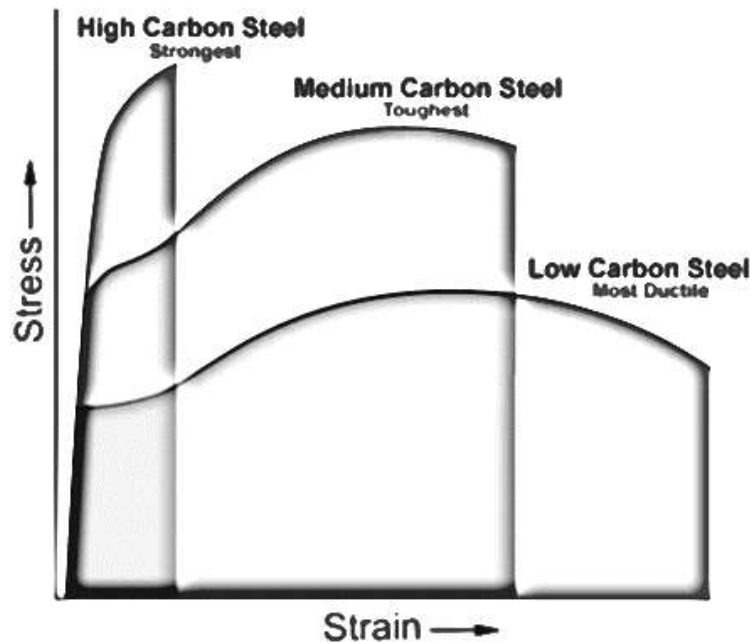
Fig. 1.1 Material toughness (adapted from "Toughness" in Nondestructive Testing (NDT) Resource Centre [2].

Numerous factors significantly influence toughness. These factors encompass:

- o Strain Rate (Rate of Loading): toughness may meet expectations under static loads but fall short under dynamic loads or impact. Generally, ductility and toughness decrease with escalating loading rates.

o   Temperature: Temperature plays a significant role in a material toughness. Lowering the temperature leads to reduced ductility and toughness.

o   Notch Effect: The notch effect is closely related to stress distribution. While a material may exhibit good toughness under uniaxial stress conditions, the presence of a notch, causing a multiaxial stress state, can lead to a material's inability to withstand simultaneous elastic and plastic deformations in various directions [2].

In the realm of materials testing, various toughness tests are standardized to generate data that corresponds to specific loading conditions or component design criteria. Three fundamental toughness properties that warrant more detailed discussion are:

- Impact Toughness

- Notch Toughness

- Fracture Toughness

These properties provide valuable insights into a material performance and suitability for diverse applications and loading scenarios [2].

1.1.3   Fracture Toughness

Fracture toughness stands as a significant measure, indicating the extent of stress necessary to advance a preexisting imperfection. This material property holds exceptional significance due to the inevitability of flaws arising during material processing, fabrication, or in-service use. These flaws may manifest as fissures, empty spaces, metallurgical inclusions, welding irregularities, design inconsistencies, or even a combination thereof. In light of the fact that engineers cannot ensure the absence of all flaws, it has become common practice to assume that some components will contain flaws of a chosen size. This assumption forms the basis

for applying the principles of linear elastic fracture mechanics (LEFM) in the design of critical components. LEFM takes into account variables such as flaw dimensions, component geometry, loading conditions, and the material's fracture toughness, all in an effort to assess a flawed ability of component to withstand catastrophic fracture [2].

The manner in which a material experiences failure, whether through ductile or brittle fracture, is intrinsically linked to its toughness. As previously elaborated, toughness is quantified by the cumulative area beneath the engineering stress-strain curve obtained from a uniaxial tensile test, as depicted in Figure 1.2. This metric denotes the quantity of energy, per unit volume, that can be imparted to a material without triggering fracture. It effectively signifies the gradual absorption of energy by the material until the point of failure. Generally, ductile materials exhibit superior toughness compared to their brittle counterparts [3].
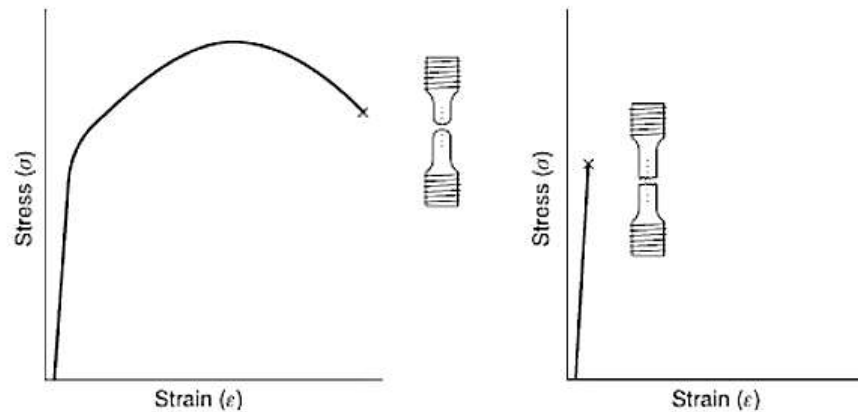
Figure. 1.2 Engineering stress-strain curve for (a) ductile fracture and (b) brittle fracture (adapted from Bhushan, 2013 [3])

1.1.3.1 Fracture toughness parameters

Fracture toughness is a property often gauged through specific tests designed for this purpose, employing parameters such as the stress-intensity factor (K), the energy release rate (G), the J

integral (J), and the crack-tip opening displacement ($CTOD$ or δ). These parameters can be quantified by assessing a single-point fracture toughness value under conditions of plain strain, including KIc, GIc, JIc, and δIc, or by constructing an entire resistance curve (R-curve). In the context of linear elastic fracture mechanics, fracture toughness is typically determined at the point near crack initiation, denoted by the plain strain fracture toughness (KIc) or the energy release rate (GIc) [4].

1.1.3.2 Variables and Specimens

Fracture toughness tests adhering to conventional standards demand elevated constraint levels at the crack tip, employing deep-cracked specimens like compact tension (CT) specimens and single-edge notch bend (SENB) specimens, detailed in ASTM E 1820-11 and illustrated in Figure 1.3 [4]. These tests encompass a comprehensive evaluation of three essential toughness parameters: K, J, and $CTOD$ within a single examination. The process involves electrical discharge machining (EDM) for initial notch creation with length a_0 and subsequent fatigue pre-cracking in a three-point bend fixture to refine the notch tip to a final length of a [5].
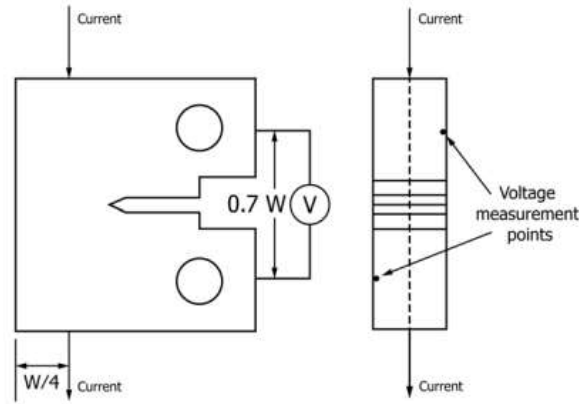
(a)
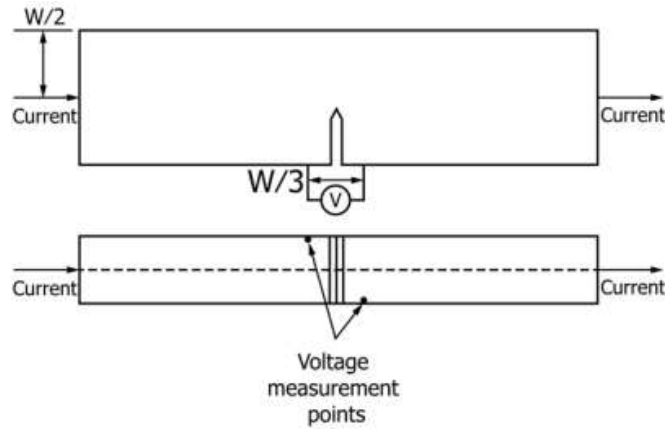
(b)

Figure. 1.3 Fracture toughness test specimens (a) compact tension specimens; (b) single edge notch bend specimens (adapted from ASTM E 1820-11) [4]

In recent years, a paradigm shift in fracture toughness testing has led to the development of tests requiring minimal constraint levels at the crack tip, involving shallow-cracked specimens as single-edge notch tension (SENT) [6]. In a study of the SENT methodology, Zhang et al. emphasized that cracked pipelines essentially function as low constraint structures because the entire ligament, even when the pipe undergoes global bending, is subjected to tensile stress [7]. Their research also established that crack depth is not a critical factor influencing the

fracture resistance of SENT specimens in pipelines characterized by small wall thickness and high toughness. It is important to note that while the SENT test method has been developed and accepted, it has not yet been standardized or incorporated into ASTM established standards. According to the BS8571:14, The clamped SENT test specimen configuration shall be as shown in Figure 1.4 [8].
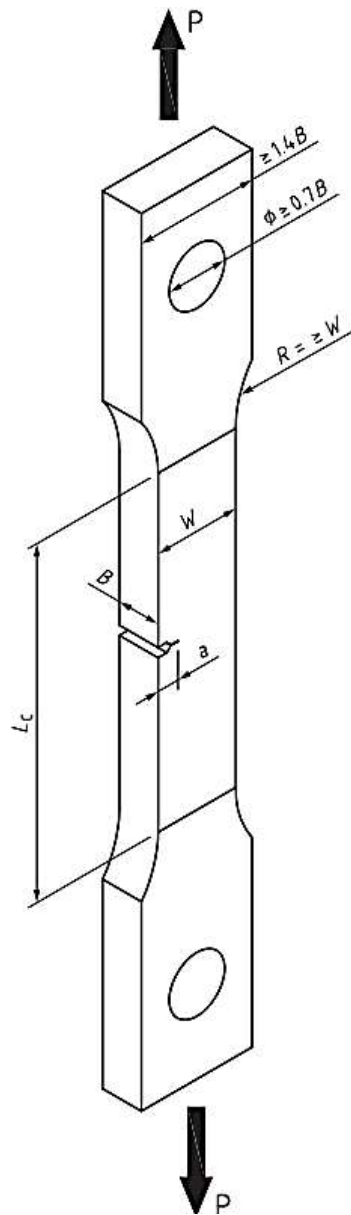
Figure. 1.4 Clamped SENT test specimen configuration (adapted from BS 8571:14) [8]

1.2 Problem Statements

Understanding the fracture behavior and toughness of pipeline steel has gained paramount importance in the contemporary era which pipelines play a pivotal role in energy transportation across many countries, notably constituting nearly 60% of energy delivery in nations such as Canada [11]. Study on the fracture toughness of pipe steel is crucial for evaluating material behavior under various conditions, and this dependency on crack tip constraint has been well-established as mentioned before [9]. In scenarios where CT tests exhibit high constraint, resulting in low fracture toughness and brittle fractures, SENT specimens present an alternative with notably higher fracture toughness owing to their low-constraint nature as depicted in Figure 1.5 [10]. The current project revolves around the exploration of SENT experimental tests and XFEM models, emphasizing the dynamic interplay between fracture toughness, crack size, and the geometry of the specimen. The magnitude of the crack size becomes a key factor influencing stress distribution around the crack tip, thereby influencing fracture toughness. As crack length extends, so does the constraint at the crack tip, potentially leading to a more brittle fracture. This underscores the necessity of exploring the relationship between toughness and crack size, aligning our methodology with the guidelines by BS 8571:14. This research adopts a multi-specimen strategy, adhering to the recommendations of BS 8571:14, to systematically explore the complex relationship between fracture toughness, crack size and specimen geometry.

This initiative is a segment of a more extensive undertaking within our research group, where we are immersed in a comprehensive project. The outstanding goal is to conduct tests on a considerable number of small-scale specimens featuring diverse geometries and crack sizes. These specimens, aim to mimic real-world conditions. The primary objective is to generate

CTOD-R or J-R curves, providing valuable insights into a material resistance to fracture under diverse conditions.

Within these experimental tests, precise measurements encompass various parameters such as crack extension, and additional displacements like CMOD and CTOD. Concurrently, the numerical analysis part of this thesis leverages the Extended Finite Element Method (XFEM) to predict fracture parameters to achieve the same toughness results as the experimental one within SENT specimens from identical pipe steel. Precision in predictions is heightened by incorporating specific fracture parameters, Maxpe and Gc.
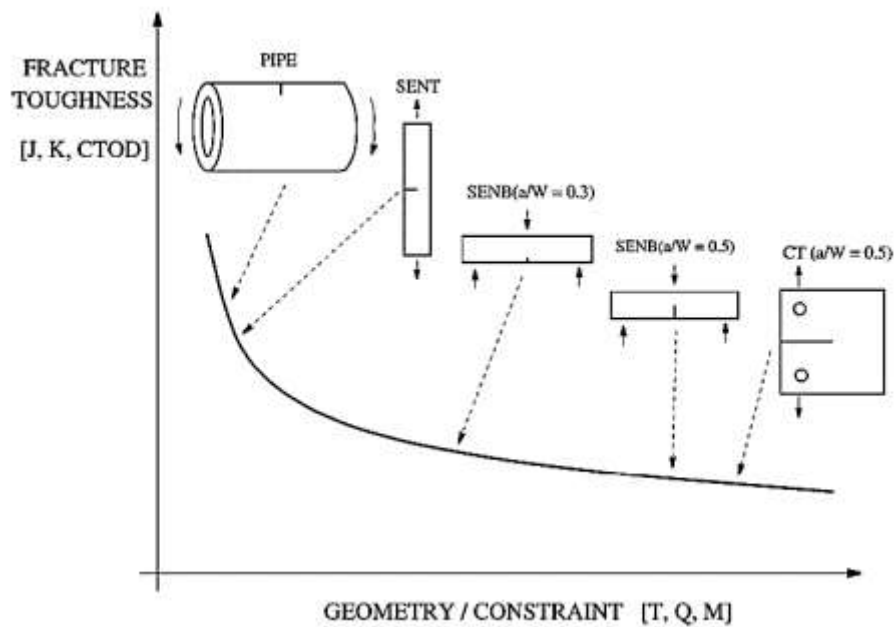
Figure 1.5. Dependence of fracture toughness on specimen geometry or crack tip constraint

1.3 Organization of Thesis

In the current chapter as the first chapter, the introduction sets the stage for the entire thesis. This section emphasizes the significance of fracture toughness as a key parameter and provides a background to the research motivation.

Secondly, Chapter 2 is dedicated to the small-scale tension (SENT) experimental tests. It commences with an exploration of the tensile and fracture properties of API X52 steel pipes. The focus is on detailing the experimental setup, methodologies employed, and the results obtained from the tests. This chapter aims to offer a comprehensive understanding of the fracture behavior under various conditions.

Thirdly, Chapter 3 focuses on the Extended Finite Element Method (XFEM) models. It elucidates the theoretical framework and details of XFEM, explaining its application in predicting crack initiation and propagation in SENT specimens fabricated from API X52 pipe steel. This section highlights specific fracture parameters, Maxpe, and Gc, and discusses how they enhance prediction accuracy. The chapter concludes with insights into the numerical analysis component of the research.

Finally, Chapter 4 serves as the conclusion of the entire thesis. It begins by summarizing the key findings from both the experimental tests and the XFEM models. The chapter then draws main accomplishments based on the collective results, offering insights into the tensile and fracture properties of API X52 steel pipes. The section proceeds by offering insights for future endeavors.

2. Single Edge Notched Tension (SENT) Test

2.1 Introduction to Tension Test

The assessment of fracture toughness in materials commonly relies on two fundamental parameters: Crack Tip Opening Displacement (CTOD) and J-integral [12]. These parameters were introduced over 50 years ago [13, 14], and have been widely adopted in fracture mechanics studies as reliable indicators of material toughness. To evaluate the fracture toughness properties of a material, various testing methods on different geometries are used [15, 16]. These including Single-Edge Notched Bending (SENB), Compact Tension (CT), and Single-Edge Notched Tension (SENT) specimens. Among all specimen geometries, SENT specimens are more suitable for simulating the pipe notch constraint, mimicking the relative crack depth observed in typical pipe defects [17]. While extensive research has been conducted on higher grades of steel such as X100 [18,19], X90 [20], X80 [21], and even X70 [19], there is a noticeable scarcity of experimental and analytical studies on lower grades such as X52. Regarding the load application technique, in order to assess the similarities and differences between single-specimen and multi-specimen techniques, several comparisons can be found in the literature. For instance, Diego et al. (2020) conducted a study on API 5L Grade X65 steel, utilizing a standard SENT specimen with a width and depth of 14 mm (B=W) in the cracking zone [19]. The findings indicate that for small crack extensions ($\Delta a \leq 1$mm), both procedures i.e., single specimen and multi-specimen techniques, yield similar fracture toughness values. This result is consistent with the comparison of these techniques reported by Pussegoda et al. for the X70 steel [19]. Current study follows to the regulations provided in BS 8571-2014, by employing the multiple specimen technique for all tests [8]. The multiple specimen technique involves using specimens with different pre-crack dimensions subjected

13

to varying levels of load, and subsequently, the resulting ductile crack extension is carefully measured and analyzed.

In the present study, our focus is on investigating the fracture toughness properties of AO Smith X52 pipe steel [22] using SENT specimens. By employing SENT specimens that closely resemble pipe notches, we can assess the behavior of material under critical loading scenarios relevant to pipeline integrity. In addition, testing of varying initial notch sizes will allow us to assess the influence of crack geometry on fracture toughness factors and determine critical points, occur after the maximum load and close to the crack initiation point, necessary for calculating CTOD and J equations based on crack extension, following the regulations of the BS 8571-2014 [8].

During the testing process, SENT specimens are subjected to a unique high-tension force applied by the testing machine until the crack at the end of the notch begins to propagate, and continuing beyond the maximum force. This test yields two essential factors: the force applied by the machine over time and the displacement of the specimen components under this force. In larger specimens, clip gauges are typically installed on either side of the crack tip or crack mouth to measure the displacement over time, providing valuable data for constructing the force-displacement diagram. However, in cases where small-sized samples are used, installing clip gauges with sufficient accuracy becomes challenging. To address this issue, this research employs the Digital Image Correlation (DIC) method, which involves capturing high-resolution images and correlating them to determine the sample's deformation under load.

2.2 Experimental Procedure

2.2.1 Test Specimens

The dimensions of SENT specimens are limited by the curvature and thickness of the pipe wall. To ensure compliance with BS 8571-2014, the following criteria for dimensions of specimens must be considered/met [8]. The specimen is recommended to be machined to a final thickness of $0.5 \leq W/B \leq 2$ mm, where B and W are respectively the thickness and width of the specimen, with a daylight grip length (H) of 10 W. These specifications ensure that the specimens meet the standard guidelines for testing. For the toughness SENT specimens, a nominal initial notch-to-width (a_0/W) ratio of $0.2 \leq a_0/W \leq 0.5$ is required. While various sources, including DNV-RP-F108 [23], CanmetMATERIALS [24], ExxonMobil [25], and BS-8571-2014 [8], offer different scenarios regarding the side grooving of specimens, it should be noted that side grooving is known to increase crack tip constraint, which is contrary to the objective of SENT specimens [26]. As per BS 8571-2014, side grooving is not a requirement for SENT specimens and is considered an optional process [8].

In the current study, the specimens are not subjected to side grooving, nor do they have fatigue pre-cracks and the notches are introduced by means of electrical discharge machining (EDM). The specimens are made from the base metal of an AO Smith long seam-welded X52 pipe (line#41) having an outside diameter (OD) of 406 mm and a wall thickness (WT) of 7.35 mm. The pipe was manufactured in the 1980s. Considering the specifications regarding specimen dimensions, the fabricated specimens are prepared using the following dimensions. The width-to-thickness ratio (W/B) is maintained at approximately 2.0. Given the prescribed width limitation of W = 7.3 mm, the corresponding value for parameter B is set to 3.7 mm. Furthermore, the daylight grip length (H) is calculated as 10 times the specimen width,

resulting in a length of 73 mm. For the a_0/W ratios of 0.2, 0.3, and 0.5, the initial notch lengths are determined as 1.46 mm, 2.19 mm, and 3.65 mm, respectively, with a consistent notch mouth size of 0.15 mm. In addition to fabricating SENT specimens, this study also involves the fabrication of five standard tensile specimens. These additional specimens are specifically designed to determine the material properties of the steel under investigation.

The orientation of the samples is YX, as illustrated in Figure 2.1 In this notation, the first letter (Y) represents the direction normal to the crack plane and the latter shows the expected direction of crack propagation within the specimen, which will align with the pipe length. The photographs of these samples are also provided in Figure 2.2. Also, Table 2.1 indicates the number of specimens tested for each initial notch size. In addition to SENT specimens, five rectangular standard tensile specimens are designed following the guidelines of ASTM E8/E8M - 11 [27] to obtain the material properties of the X52 steel grade. According to the regulations outlined in the mentioned standard, the specimens are designed with the following dimensions: total length of 100mm, grip section length of 32mm, width of 6mm, and thickness of 6mm.

Table 2.1 SENT test specimens

Initial Notch Size (a_0/W)	Number of specimens
0.2	3
0.3	3
0.5	3
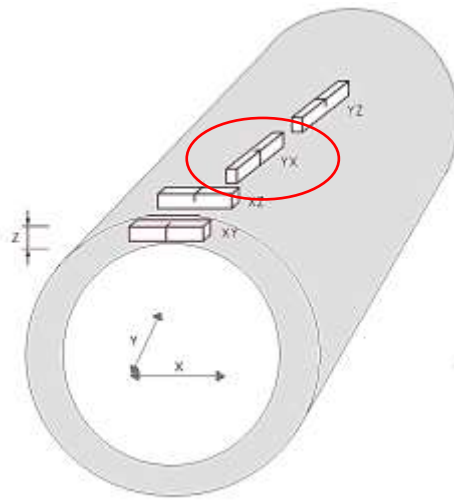
Figure 2.1 Crack plane orientation code for fracture toughness specimens of the base metal (adapted from BS8571-14) [8]
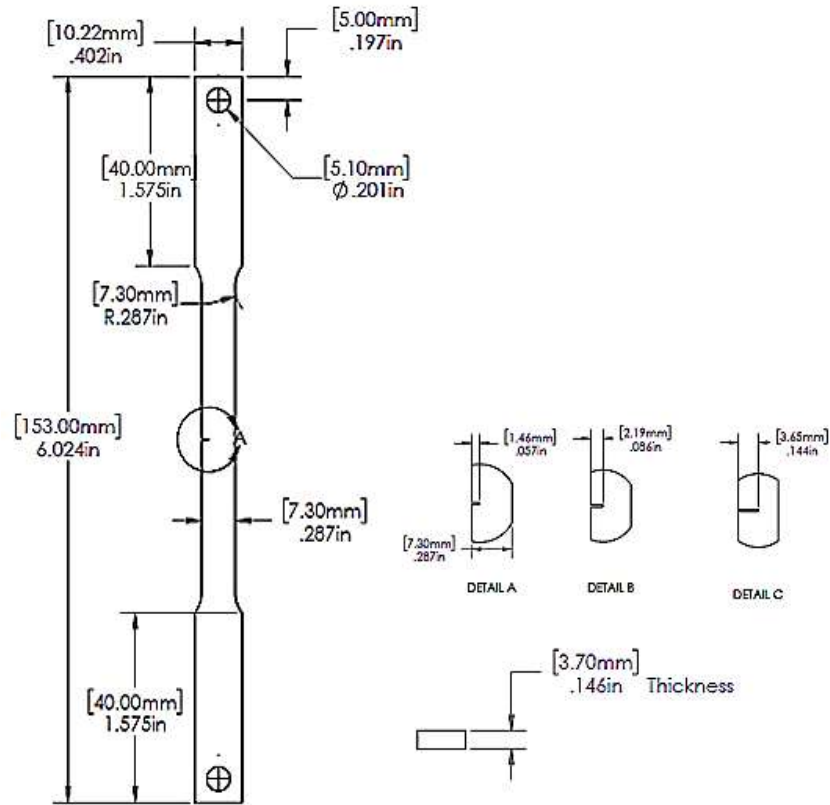
(a)

(b)

Figure 2.2 (a) Engineering drawing of the specimens (b) Photograph of manufactured SENT specimens:

(b1) a_0/W=0.20, (b2) a_0/W = 0.30, and (b3) a_0/W = 0.50

2.2.2 Test Equipment and Setup

The experimental setup for the SENT specimens comprises the MTS Criterion Universal Testing Systems (with a load capacity of 100 KN) as shown in Figure 2.3. The MTS testing machine consists of two robust supports for the load frame, a load cell responsible for converting forces into digital signals, a crosshead, and grip fixtures.

DIC system, consists of two powerful cameras, high-resolution lenses, a light source, a computer, DIC software, and calibration kits.

2.2.3 DIC system setup

A schematic diagram of the DIC system setup is presented in Figure 2.4. The cameras are placed at a fixed distance and angle from the specimen and are connected to the computer running the DIC software. The specimen is then loaded while the cameras capture images of its surface at specific intervals. The software uses these images to track the movement of speckle patterns on the specimen's surface and calculates the displacement and strain fields. The light source is used to ensure that the concentrated brightness remains consistent throughout the test.

The experimental process commenced with specimen preparation, which involves coating the entire surface of the specimen with pure white color. Subsequently, black dots were sprayed onto the white surface from a distance of about 50 - 60 cm. The speckles resulting from the spraying process were very small and had an approximate distance of less than 1 mm from each other. Moreover, they were uniformly distributed across the entire specimen [28].

In certain scenarios, such as slow, quasi-static tests and moderate aperture, ambient room lighting may provide sufficient illumination. However, in most cases, additional lighting is

necessary to achieve optimal contrast with a given aperture and exposure time. In such instances, white light or light of specific wavelengths or wavelength bands may be utilized. Ensuring appropriate lighting conditions during testing is crucial for capturing high-quality images. Therefore, specialized lighting equipment must be employed to maintain a constant and stable illumination across the entire specimen throughout the experiment. In most of the tests, the standing light source generating a wide white brightness was utilized. While this lighting method appeared sufficient for initial demo testing, it was soon discovered that when the specimen deformed due to tensile loading, the light source cast a wide shadow in the background. Moreover, there was no recognizable difference between the brightness of the specimen surface and the surrounding testing area due to the lack of concentrated illumination. These issues could cause the software not to be able to recognize certain portions of the specimen, such as the area close to the crack tip and mouth, and thus missing them in the final analysis and were resolved by using a concentrated laser lighting source in the main phase of the tests.

(a)

(b)

Figure 2.3 (a) MTS test machine and (b) Test setup
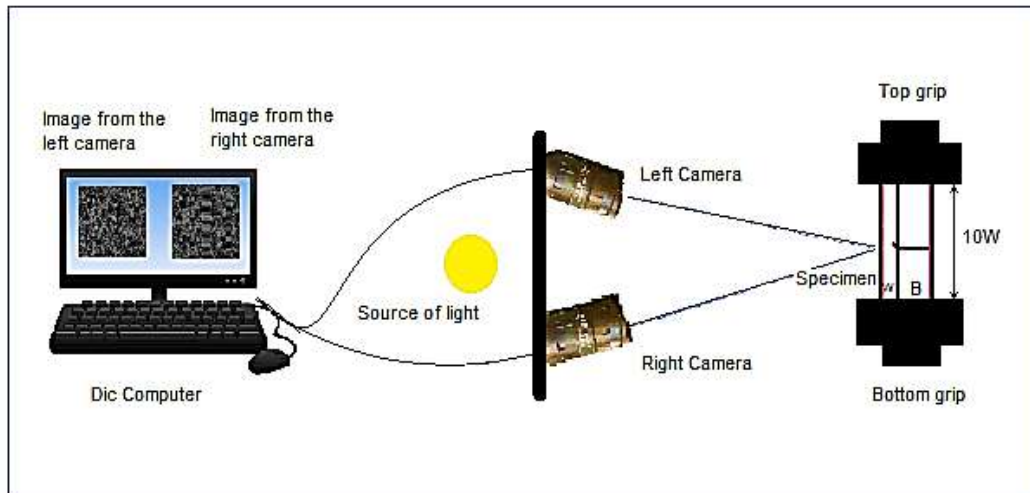
Figure 2.4 Schematic of Digital Image Correlation system setup

In the course of the experiment, two cameras with a resolution of 2448 × 2048 pixels each, capture images of the specimen simultaneously. The determination of the displacement of each point in the x, y, and z directions is carried out by correlating the digital images utilizing specialized software called VIC-3D [29]. The cameras used for this experimental test are (Point Grey GRAS-50S5M-C), and the high-resolution lenses are Nikon Macro 100F2-8D.

The other tool employed to setup the system is the standard calibration kit. The objective of calibrating a DIC system is twofold: First, to determine the image scale, which refers to the number of pixels in the image that correspond to a specific physical distance on the test piece, and to correct for any lens distortions. Second, to establish both the intrinsic camera parameters, including focal length, image center and extrinsic parameters of the stereo-DIC system, such as stereo-angle, distance between cameras, and distance from cameras to object. These calibrations are crucial for accurate and reliable measurements during the DIC analysis [30].

Once the calibration is completed, only a few parameters can be modified, and all the other conditions should remain constant throughout the test. The selection of an appropriate calibration kit for a DIC system is critical for achieving accurate measurements. Factors such as the distance between the two cameras, specimen size, speckle size and object-to-camera distance should be taken into consideration when choosing a calibration kit. For the purposes of this study, a 9×9 glass-type calibration kit with a speckle size of 1.34 mm, as shown in the top-right corner of Figure 2.5a, is utilized to accommodate the specific requirements of the SENT standard tensile tests. Figure 2.5b also presents the DIC software recognition of the dots on the calibration kit as valid points.
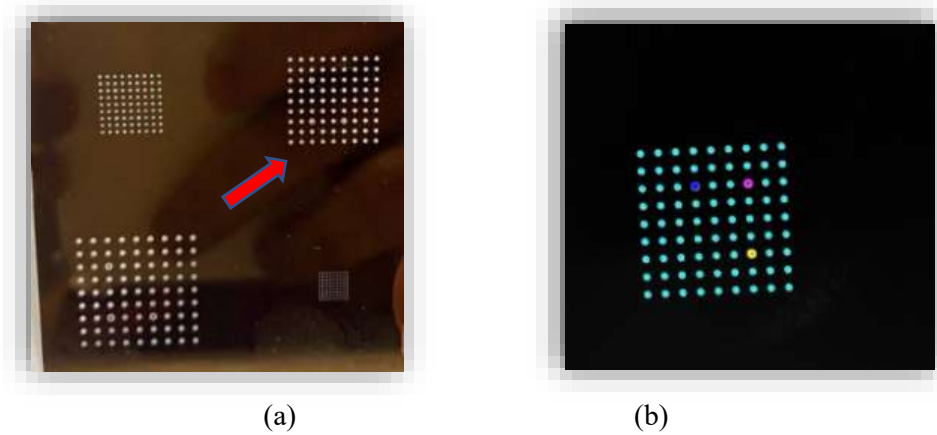
Figure 2.5 (a) DIC calibration kits 9×9 (1.34 mm) (b) Recognized dots by cameras

2.2.4 Test Procedure

The standard procedure for conducting a tensile test involves placing a specimen in a testing machine, applying a uniaxial tensile load, and measuring the deformation until the specimen fractures. The test can provide information on several material properties such as yield strength, ultimate tensile strength, elongation at fracture, Young's modulus, and stress-strain curves. The tensile tests are conducted using two different loading rates. The loading rate for the first specimen was 0.1 mm/min, with the DIC system capturing two images per second, resulting in over 11,000 images. For the second specimen, the loading rate was increased to 0.3 mm/min, with the DIC system recording one image per second. This reduced the total number of images to between 1800 to 2000, saving, saving testing and processing time. Comparison of the results from the two loading rates show no significant differences, so the second loading rate and one image per second are used for the remaining tensile specimens.

In the case of a SENT test, the testing procedure closely resembles that of the initial tensile specimen, with a loading rate of 0.1 mm per minute and the image capture rate of two per second. A total of approximately 1200 to 1500 snapshots per experiment are recorded. The

crack is then propagated under a tensile load until the specimen fractures. The load and deformation data are subsequently utilized to calculate the fracture toughness of the material. Since the SENT specimens are specifically designed to create a crack along the initial notch location, in order to post-process the data, only the areas above and below the notch are analyzed with DIC system. Below is an example of the speckle pattern on a %50 SENT specimen and the areas around the notch evaluated with the DIC system. (Figure 2.6a and 2.6b).
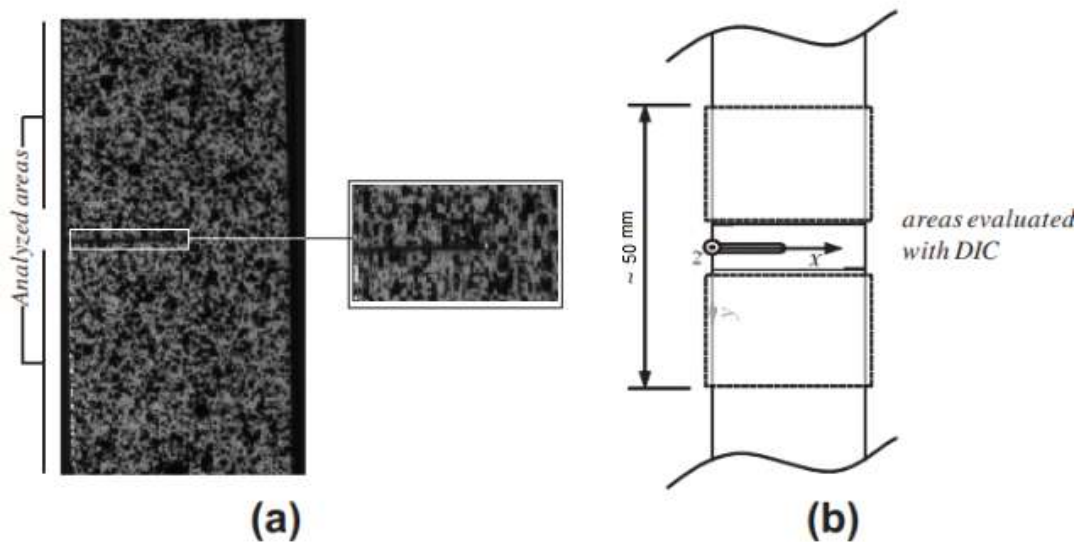
Figure 2.6 (a) An Example of speckling pattern, and (b) DIC local coordinate system considered

2.2.5 Data Processing

The initial data processing step in the Vic 3D software involves loading the calibration images and determining the scale of the points. The captured images from the tensile test are then loaded, and the desired boundaries on the first image are delineated. Scaling of the speckled area within the selected region is achieved using a reference point near the crack tip. The software tools can be used to quickly assess specimen dimensions and compare them with

actual values for measurement accuracy verification. Fundamental to the measurement requirements are the displacements of points in the vicinity of the crack during the test, which are used for producing the desired curves or for calculating parameters such as the J integral. Among these displacements, the crack tip opening displacement (CTOD) and the crack mouth opening displacement (CMOD) are significant. However, a common challenge in such measurements is the exclusion of points near the crack mouth during the process. To mitigate limitations in direct CMOD measurement using correlation methods, a clip gauge with two knife edges is usually employed to measure displacements between clips. However, in this study, the use of high-resolution lenses, an optimized setup, and focused laser light on the crack growth area eliminates missing points at the edges. Consequently, CMOD can be directly extracted using the Vic 3D software by accurately setting two measurement points precisely at the edges of the notch/crack (Figure 2.7a). Following the GKSS test procedure, the conventional arrangement for CTOD measurement involves placing two points at the top and bottom of the initial notch, with clip gauge knives positioned to measure vertical displacement [36]. Since this study employs the DIC system without clip gauges, careful selection of these two points in the initial image is required. Subsequently, the Vic 3D software automatically measures displacement throughout the correlation process (Figure 2.7).

In this study, the crack growth for each specimen is also assessed using VIC-3D software, which incorporates both measured strain contours and length measuring tools. Initially, an automated strain measurement is conducted within the designated Area of Interest (AOI), which here is the bottom part of the specimen daylight, resulting in comprehensive strain distribution data along the crack growth path. This crucial step lays the foundation for subsequent crack growth analysis.

(a)   (b)
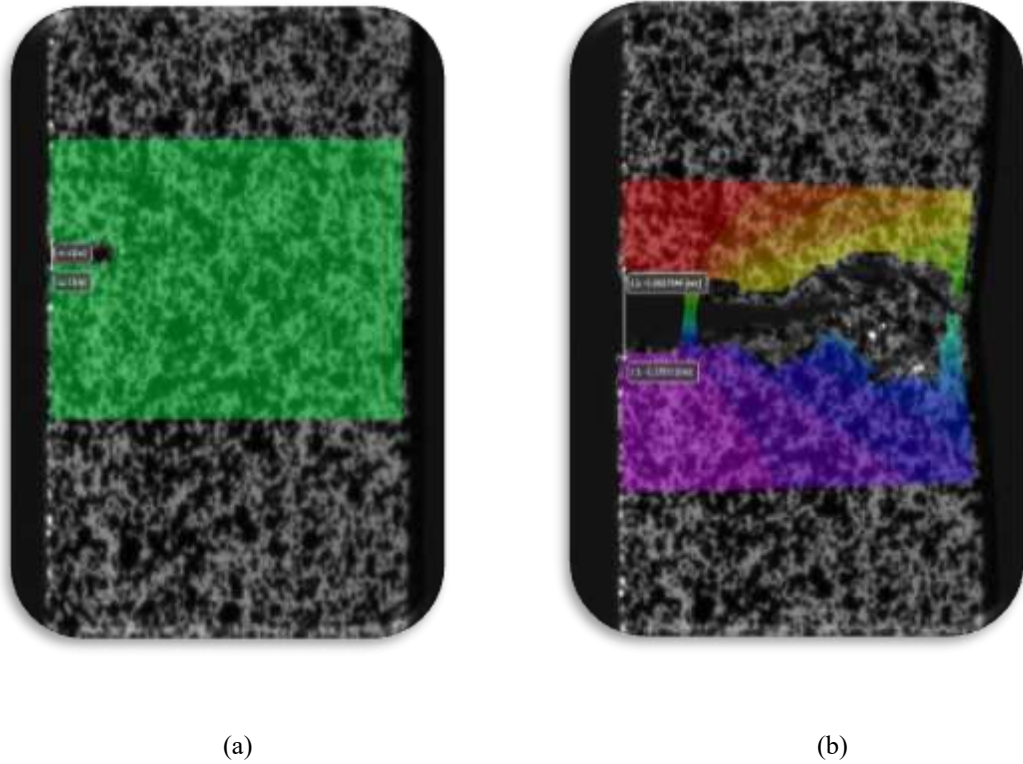
Figure 2.7 (a) Image number 1 from the correlated images of the first specimen with a_0/W=0.2 and, (b) Image number 1204 from the correlated images of the first specimen with a_0/W=0.2

The methodology involves monitoring changes in crack length between consecutive images and calculating the average crack length from three images preceding and three images following the desired image. The selection of a point locating right below the crack tip is vital, as it serves as a reference for tracking crack growth during the loading process. Before selecting this reference point, the coordinate origin (0, 0, 0) is redefined at the crack tip, ensuring precise and consistent measurements throughout the study.

To determine Δa and locate the new crack tip, strain contours of specimens with three different initial notch sizes were carefully examined. The strain contours included measurements of strain along the X direction (e_{xx}), strain in the Y direction (e_{yy}), and shear strain (e_{xy}). The VIC-

3D software facilitated the identification of Max (Maximum tension strain) and Min (Maximum compression strain) values for each contour plot at every processed image.

The process involved finding the most relevant strain contour with the new crack tip location to measuring the horizontal distance between the new crack tip and the reference point mentioned earlier. To achieve this, the software analyzes Max and Min value points at consecutive images. Among the evaluated contours, the location of the Max point of strain contour perpendicular to the crack growth path (e_{yy}) well indicated the new crack tip position. Starting from the initial image of crack propagation, the horizontal distance between the reference point and this Max point along the X direction provides the $\mathit{\Delta a}$ value. To accomplish this, the contour variable is switched to length measurement along the X direction first.

An illustrative example of applying this method is presented in the "Results" section. The process of utilizing strain contours to determine $\mathit{\Delta a}$ for a specific SENT specimen with a particular initial notch size is thoroughly demonstrated and analyzed. This example highlights the effectiveness and reliability of the new method in accurately capturing crack growth behavior and obtaining valuable fracture parameters. Notably, this approach is being employed in this project for the first time, further enhancing its significance in fracture mechanics studies.

In addition to evaluating the toughness parameters of SENT specimens, the data from dog-bone standard tensile tests is also processed to determine the true and engineering stress-strain curves. The engineering strain values are extracted through the utilization of strain measurement tools at VIC-3D software. To achieve this, two points are chosen on either side of the crack growth path, each located 12.5 mm away from the centerline and totally 25 mm apart from each other, adhering to the guidelines provided by ASTM E8/E8M – 11 [27]. The

line that passes through these selected points is used as the gauge length along the Y direction for strain calculation. Subsequently, the "Engineering strain" tensor type is selected, and all the images captured throughout the test are taken into consideration for detailed analysis. The engineering stress values are determined by dividing the load applied by the testing machine with the initial/original cross-sectional area within the gauge length of the tensile specimens.

Substitution of engineering strain and stress values in equations (1) and (2) yields respectively the true strain (ε_t) and true stress (σ_t) values, which are then used for plotting the true stress-strain curve in Figure 8. The mentioned conversion has been employed in numerous studies, among which the work of Tu et al. [31] can be referenced.

$$\varepsilon_t = \ln(1 + \varepsilon_e) \tag{1}$$

$$\sigma_t = \sigma_e(1 + \varepsilon_e) \tag{2}$$

The parameters σ_t and ε_t represent the true stress and true strain, respectively, while the parameters σ_e and ε_e correspond to the engineering stress and engineering strain, respectively [31].

2.2.5.1 J-integral calculation

For the calculation of J-integral from CMOD for a clamped SENT specimen with the W/B ratio of 2.0, the method outlined in the BS 8571-14 guidelines method is followed as below [8]:

$$J = J_{el} + J_{pl} \tag{3}$$

$$J = \frac{K^2(1 - \nu^2)}{E} + \left(\frac{\eta_{CMOD}}{W - a}\right)\left(\frac{U_p}{B_N}\right) \tag{4}$$

and:

$$K = \left[\frac{p\sqrt{\pi a}}{(B \times B_N)^{\frac{1}{2}} W} \right] G\left(\frac{a}{W}\right) \tag{5}$$

where:

$$G\left(\frac{a}{W}\right) = \sum_1^{12} t_i \left(\frac{a}{W}\right)^{i-1} \tag{6}$$

$$\eta_{CMOD} = \sum_1^{10} \varphi_i \left(\frac{a}{W}\right)^i \tag{7}$$

where K is the elastic stress intensity factor, J_{el} is the elastic component of J, J_{pl} is the plastic component of J, and η_{CMOD} is a dimensionless function of geometry. In addition, t_i and φ_i are constant values which are taken from tables provided in BS 8571-14 [8].

Additionally, an important factor to consider is U_p, which refers to the plastic area under the load versus CMOD curve. In the case of adopting the single specimen method (unloading compliance method) the area under this curve should be calculated from the initial point up to the desired unloading location. After computing the total area under the curve, the elastic area must be subtracted to isolate the plastic area value. The same procedure applies to the multi-specimen technic, with the difference that, in this method, the critical point (i.e., the point after the maximum load, at the crack initiation) is selected to calculate the area under the curve.

2.3   Results and Analysis

2.3.1 Standard tensile test

The stress-strain behavior of the test material, API 5L X52 pipe steel, is depicted in Figure 2.8. This curve represents as an average of the stress-strain curves obtained from five

individual tensile specimens. Table 2.2 provides a summary of the engineering mechanical properties specific to the pipeline steel.
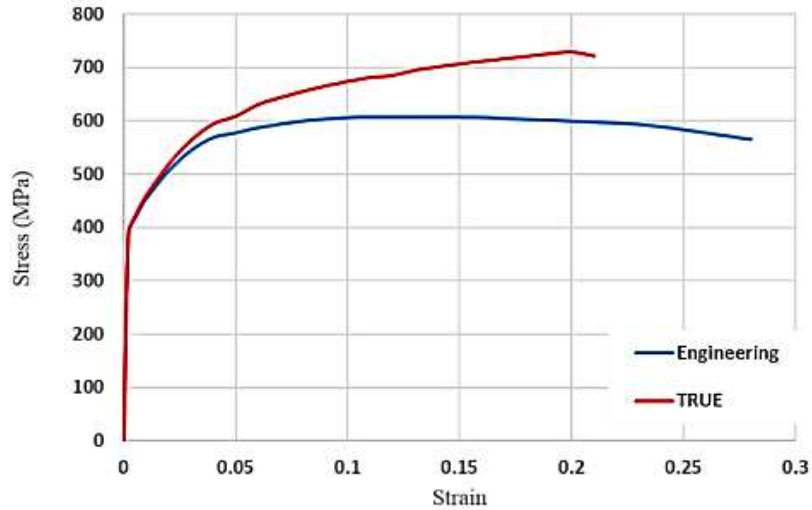
Figure 2.8 X52 pipe steel stress vs. strain curves.

Table 2.2 X52 pipe steel mechanical properties.

Sample	Rectangular Transverse Specimen cut from L41 MP699 (tested at UofA mechanical engineering lab)
0.2% Yield Stress (MPa)	420
Ultimate Tensile Stress (MPa)	607.5
Young's Modulus (MPa)	192531

2.3.2 Δa measurments using e_{yy} strain contours

An exceptional feature of this study lies in the approach employed to measure Δa using strain contours in Vic 3D software for crack growth analysis, which has not been previously presented. Figure 2.9 visually depicts the Δa measurement process for a specimen with

a_0/W=0.2. As outlined in the "Data Processing" section, the selected point at the crack tip in the first image serves as the reference point, and the displacement of any points with the label of the maximum value on the e_{yy} strain contour from this reference point along the crack growth path represents the Δa value. The corresponding Δa values for the specific sequence of images (number 1, 550, 800, 1000, 1100, 1200) are recorded as follows: 0 mm, 0.215 mm, 0.735 mm, 1.656 mm, 2.576 mm, and 3.165 mm, respectively.
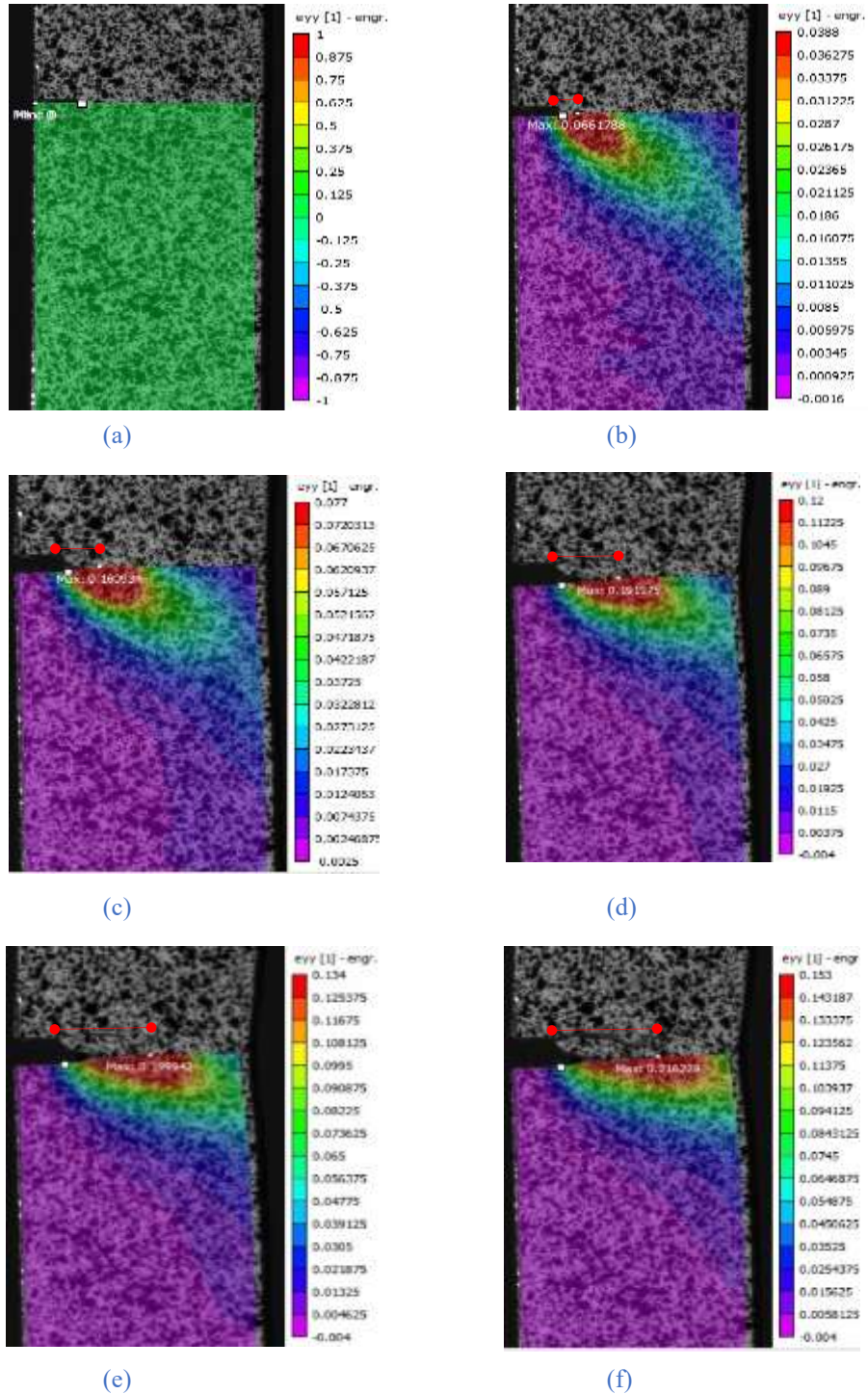
Figure 2.9 An example of *Δa* measurement for *a₀/W* = 0.2 SENT specimen; (a) Image number 1, (b) Image number 550, (c) Image number 800, (d) Image number 1000, (e) Image number 1100, (f) Image number 1200

2.3.3   Force-CTOD and Force-CMOD curves

Through the correlation process utilizing the DIC system and test data, the Force-CTOD and Force-CMOD curves are obtained for each of the nine specimens tested in this study. The MTS testing machine provides load and global displacement data for the specimens at incremental steps, with the increments being adjusted based on the image capturing rate of the DIC. Thus, corresponding load values are available for each step in-relation to the correlated images in the Vic 3D software. The combination of these results for each specimen yields the curves is shown in Figure 2.10 and Figure 2.11. It is evident from Figure 2.10 that all three specimens within each notch size category exhibit remarkable agreement with one another. Their overall behavior, particularly in the initial linear region, yielding point, and peak load, demonstrates significant similarity within each category. Specimens with a_0/W=0.2, 0.3, and 0.5 reach a peak load of approximately 11.5 kN, 10 kN, and 7 kN, respectively. The critical CTOD values for all nine specimens fall within the range of 0.07 mm to 0.15 mm. Figure 2.12 illustrates the scatter plot of critical points at maximum load for all specimens.

The CTOD values at maximum load for three notch sizes reveal insights into the ductility of material across these different notch sizes. Higher CTOD values generally mean better resistance to crack growth and increased ductility. In this study, a positive link between increasing CTOD values from $a_0/w = 0.5$ to $a_0/w = 0.3$ and $a_0/w = 0.2$ can be observed, suggesting higher CTOD is associated with greater ductility. This aligns with the idea that specimens with higher CTOD values can undergo more deformation before fracturing, indicating a more ductile response. This pattern is consistent with findings in other studies, like the one by Ohata et al. on X80 steels with similar notch sizes [53].

The Force-CMOD curves exhibit a similar agreement with the distinction that in the specimens with a_0/W=0.5, the critical crack mouth opening displacement occurs farther from the other two crack sizes, standing at approximately 0.35 mm, while the critical CMOD values of the other two crack sizes lie in the range of 0.17 to 0.2 mm. Another notable aspect of these curves is the uniformity of the results across all nine tests, except in the tail region, which signifies the energy absorption phase. The CTOD values obtained from the Force-CTOD curve at critical points for each specimen directly reflect the toughness assessment, as these points illustrate the material's resistance to crack propagation in conjunction with the corresponding crack extension. Similarly, the CMOD values extracted from the Force-CMOD curve provide insights into the overall deformation and displacement near the crack mouth. The CMOD values at the critical points of each specimen are utilized to determine one of the key factors in calculating the J-integral at those points. Drawing the J-integral versus the corresponding crack extension provides an additional means of assessing the material's toughness property.

2.3.4 R-curves (CTOD-Δa and J- Δa)

The J-resistance and CTOD-resistance underwent curve fitting through the utilization of power-law regression curves. The regression procedure for SENT test results is performed based on the guidelines prescribed in BS 8571-14 [8]. During the regression analysis, data points falling within the exclusion limits of 0.2 mm and 2 mm are taken into account. However, it is important to note that due to the limitations imposed by small-scale specimen testing in this study, the critical crack extensions of most specimens fall close to the 0.2 mm line. According to Figure 2.13 and Figure 2.14, two data points show a critical CTOD value smaller than the 0.2 mm threshold and, as a result, are excluded from the power fitting

regression calculation according to BS 8571-14 [8]. This observation highlights the fact that in the case of small-scale specimen geometries and different notch sizes, the critical points at maximum load levels occur within a narrow range of crack extension values.
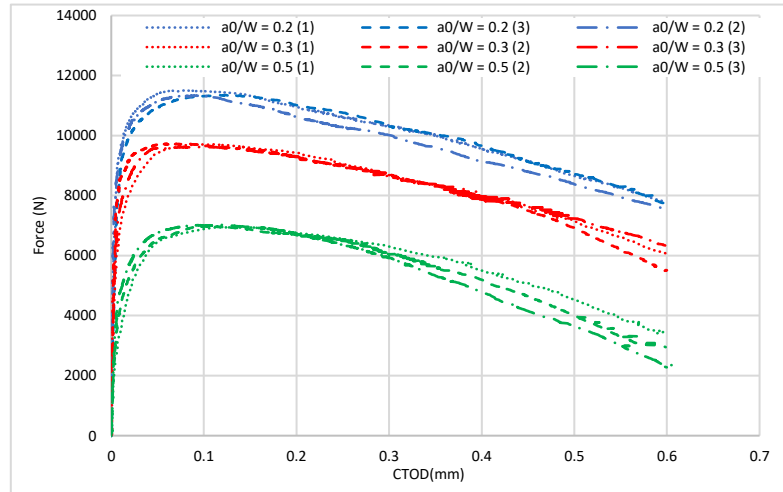
Figure 2.10 Force-CTOD curves
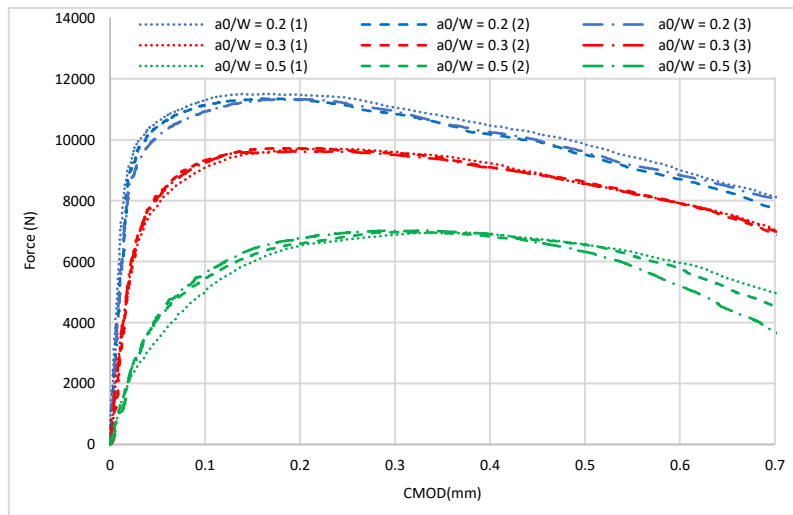
Figure 2.11 Force-CMOD curves
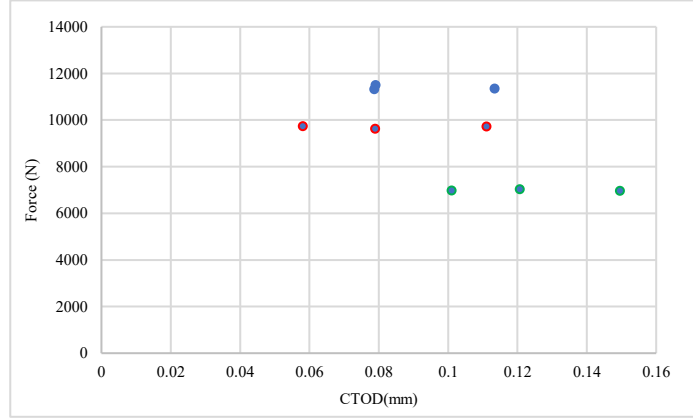
Figure 2.12 Scatter plot for the CTOD value corresponding to the maximum load for each test (critical points)

The J-resistance curve fitting plot exhibits a similar trend, wherein a limited range of crack extension alignes with the stable crack initiation points for CTOD. As a result, different energy values are computed for each point based on their respective positions in the Force-CMOD curve. In view of these observations and following the guidelines specified in BS 8571-14, the general equation for calculating J or CTOD based on Δa can be expressed as follows [8]:

$$J \text{ or } CTOD = C_1 \Delta a^{C2} \tag{8}$$

where Δa is crack extension, and $C1$ and $C2$ are regression constants [28]. Equations (9 and (10) represent the mathematical expressions derived from the stable crack initiation points observe on the CTOD-Δa and J-Δa curves, respectively [8]. These equations are used to plot the corresponding curves, as illustrated in Figure 2.13 and Figure 2.14, respectively.

$$CTOD = 0.3117 \Delta a^{0.91598} \tag{9}$$

$$J = 344.612 \Delta a^{0.74109} \tag{10}$$
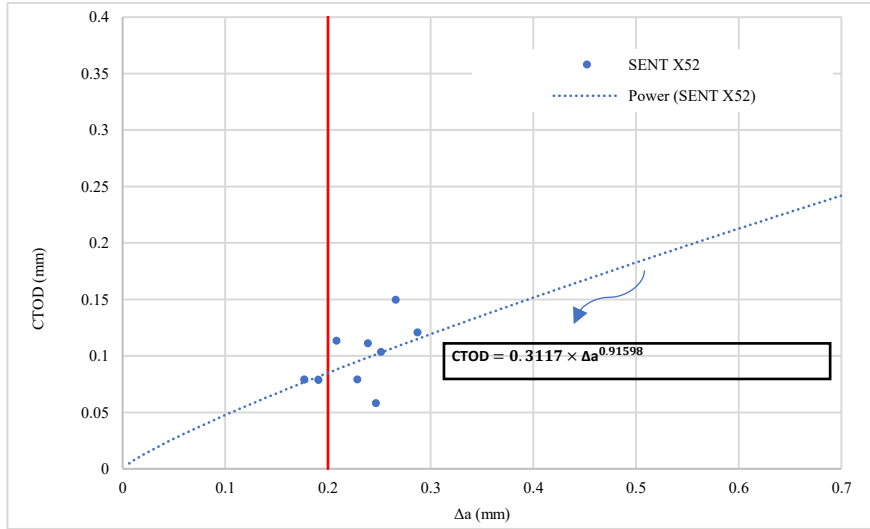
Figure 2.13 CTOD- Δa curve obtained from stable crack initiation points for X52 steel specimens
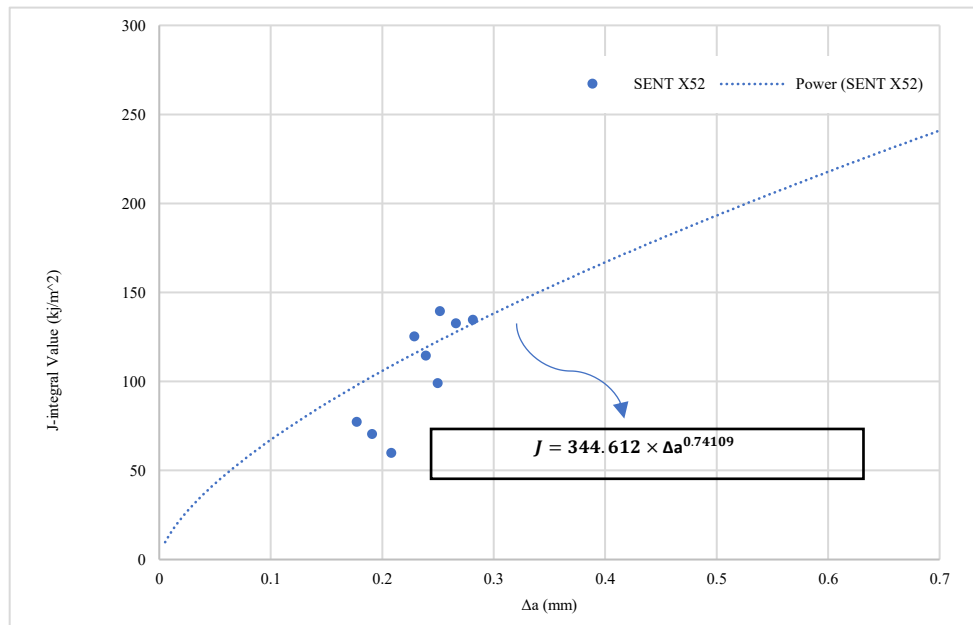
Figure 2.14 J- Δa curve obtained from stable crack initiation points for X52 steel specimens

In contrast to conventional standards that recommend a single point per specimen in the multi-specimen technique, our study took a more detailed approach. We measured CTOD-Δa at various points (0.2-2.0 mm) for each of the nine specimens, going some steps beyond standard practices to compare the behavior of each single specimen with the method provided by the

standard for the whole process. The resulting curve, depicted in Figure 2.15, showed excellent agreement with the CTOD-Δa curve based on stable crack initiation points (Figure 2.13). The black power fitting plot in Figure 2.15, derived from the same points as Figure 2.13, effectively captures the crack growth behavior of each specimen, enhancing our understanding of what concept the Figure 2.13 wants to transfer.

Notably, the black power fitting plot shows a tendency to closely adhere to results from %20 and %30 crack sizes more than %50. This observation underscores a key rationale behind standards favoring the selection of a single point in the crack initiation stage as a representative measure of specimen behavior, consolidating the entire material behavior based on these critical points.
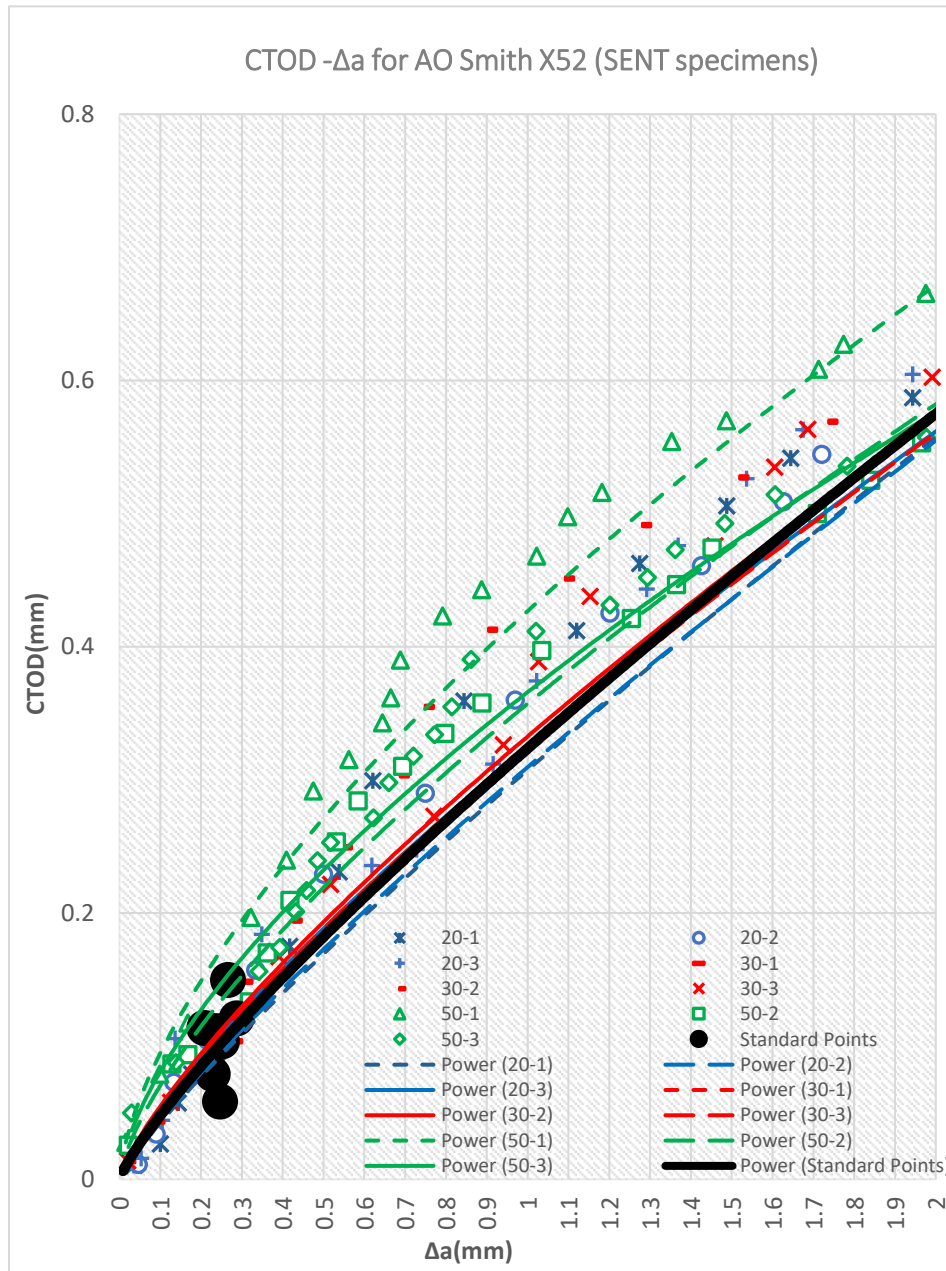
Figure 2.15 CTOD-Δa Analysis of each specimen

2.4 Discussion

The primary objective of this chapter was to determine the fracture properties of SENT specimens extracted from the base metal of X52 steel pipe. To achieve this, we utilized a

multiple specimen technique, which is widely recognized as a common method for evaluating R-curves, as specified in BS8571:2014. Both the nine SENT and five rectangular standard tensile tests were conducted using DIC system, enabling us to derive essential parameters such as CTOD, CMOD, and J plus the material properties of this steel grade. However, the key distinction between our study and other similar investigations, lies in the method of crack growth value extraction. For instance, in tests conducted by Tang et al. on X80 SENT specimens [32], or the similar study on X42 steel carried out by Ameli et al. [33], the nine average point method in accordance with ISO 12135 [34] was employed. In contrast, in the current study, we employed the direct measurement approach using strain contours, showcasing the innovation of this methodology.

The comparison of CTOD-Δa results depicted in Figure 2.16 provides insights into the relative performance of grade X52 steel compared to higher steel grades such as X65, X80, X90, and X100. It is noteworthy that the availability of experimental research specifically focused on grade X52 steel is limited, prompting the need to compare the results with those obtained from other grades. As the crack extension increases, the differences and variations in the toughness characteristics among different steel grades become more pronounced. Additionally, it is important to emphasize that the geometries of the specimens used in the experimental tests conducted in the previous studies predominantly featured *B/W*=1.0 with dimensions ranging from 12mm to 17mm which is larger than those examined in the current study. This range of dimensions was selected due to the constraints imposed by their available pipe samples and the inherent challenges associated with obtaining larger sizes of SENT specimens. Furthermore, it is worth noting that a similar comparison has been conducted for another

relevant toughness parameter, J, further enriching the understanding of the material's performance.

Figure 2.17 provides a comparison of the *J* versus *Δa* behavior of X100 steel, tested by Weeks et al. [18] and Tyson et al. (2014) [35], plus X70 steel tested by Pussegoda et al. (2012) [21]. This comparative analysis allows for a deeper understanding of the toughness characteristics exhibited by different steel grades. The power fitting result obtained from the current study on the J-Δa curve exhibits a strong correlation with the curves representing the stronger steel grades. The similarity in the trends and behavior of the J-Δa curves across the different steel grades are evident. These findings contribute to the body of knowledge on the mechanical behavior of X52 steel and its comparison with other steel grades in the pipeline industry, enabling researchers and engineers to make informed decisions regarding material selection, design, repair and maintenance.

Furthermore, in our study, the critical points (points with maximum load values) were found to occur within the crack extension range of 0.18 to 0.3. This observation aligns with findings from other studies in the literature, such as the investigation conducted by Dong et al. (2014) on X70 steel SENT specimens [37]. However, it is important to note that Dong et al. employed the unloading compliance technique on several specimens, and their results indicated critical points with crack extension values ranging from 0.2mm to 0.4mm. The consistency of our critical point values within a similar crack extension range reaffirms the reliability of our experimental data.
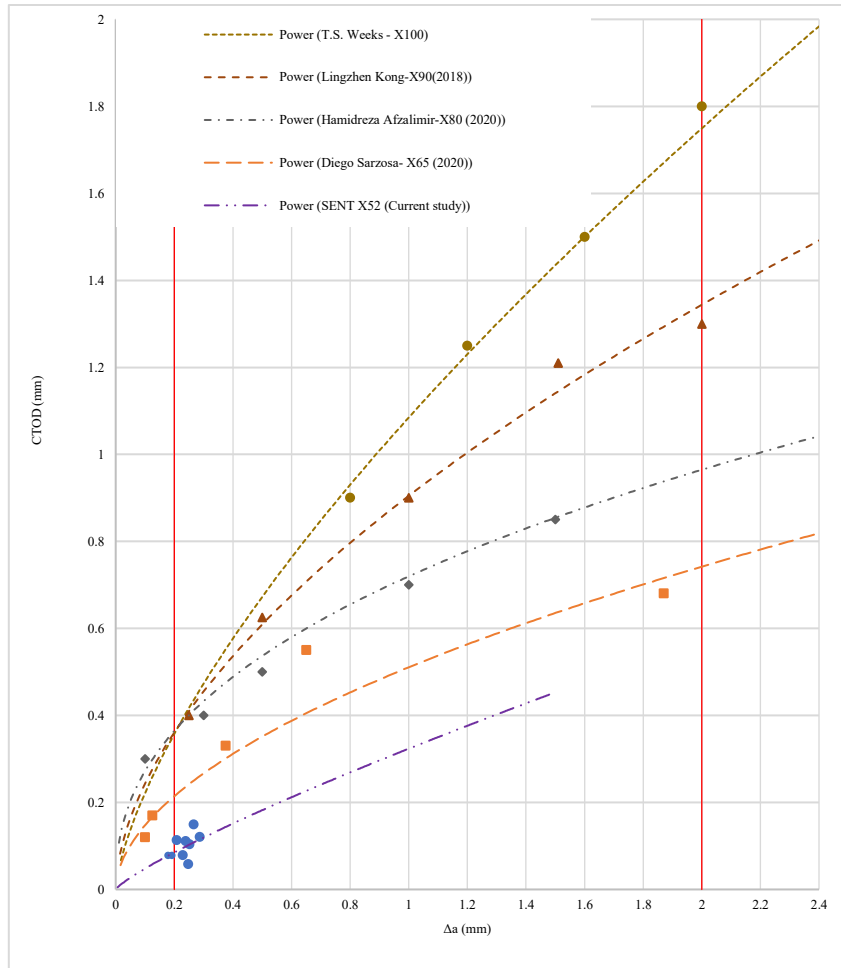
Figure 2.16 Comparison of CTOD- Δa for various pipe steels [data from 38, 21, 35, 20]
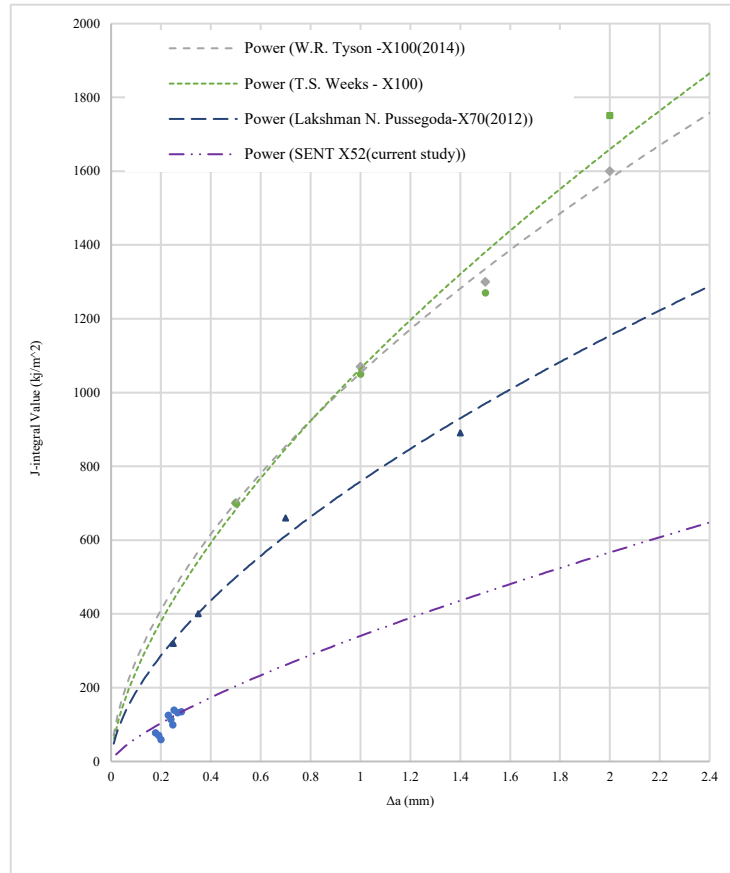
Figure 2.17 Comparison of J- Δa for various pipe steels [data from 18, 35, 19]

2.5 Conclusion

The study involves a total of nine clamped SENT specimens, containing three different initial notch sizes, with three specimens for each notch size ($a_0/W = 0.20$, $a_0/W = 0.30$, and $a_0/W = 0.50$). The specimens have a consistent geometry with thickness $B = 0.5$, width $W = 3.7$ mm, and daylight grip length over width ratio $H/W = 10$. The testing procedure and calculation of crack length, J, and CTOD follows the guidelines outlined in BS 8571-2014. The experimental approach employs the multi-specimen technique, with the critical points at maximum load serving as the key parameters for determining the fracture toughness properties of the steel material. During the test, the digital image correlation system is utilized for displacement measurement and subsequent analysis of the data. The Force-CTOD, Force-CMOD, CTOD-

Δa, and *J-Δa* curves are plotted for further comparisons and calculations of toughness equations and are compared with similar experimental tests on the higher grade of material in the literature. The main conclusions of this study are as follows:

- The Force-CTOD curves exhibit consistent behavior across different initial crack sizes, showing similar trends in the elastic region, yielding point, and energy absorption phase. The ratio of maximum loads to crack sizes follows a reasonable pattern.

- The Force-CMOD curve shows that specimens with a_0/W=0.5 have larger CMOD values at critical points compared to other crack sizes, indicating a significant influence of crack size on crack mouth displacement. The critical point for all specimens falls within the range of 0.2 mm to 0.35 mm of CMOD values. The similar points in other grades such as X65 occur within the range of 0.6 mm to 0.7 mm for specimens with $a_0/W = 0.3$ [38].

- The J- and CTOD-R curves in this study exhibit similar trends and behavior to higher-grade steels, indicating comparable fracture characteristics. The direct measurement of CTOD-R during testing provides more reliable results compared to the calculated J value, which involves multiple equations and potential errors. In comparing different steel grades, at $Δa = 2mm$, the CTOD ratio is approximately 2.0 for X80/X52 steel and almost 3.0 for X100/X52 steel. Similarly, the J-integral value ratio is 1.7 for X70/X52 steel and 3.1 for X100/X52 steel. These ratios highlight notable differences in fracture toughness among the steel grades.

This study is a component of a larger project aimed at comprehensively understanding the toughness properties and fracture behavior of X52 pipe steel from testing with various loading

constraints, including SENB (Single-Edge Notched Bend), CT (Compact Tension), and CVN (Charpy V-Notch) tests. Furthermore, finite element simulations are conducted to provide further insights into the mechanical response of pipe steels. The findings from these ongoing investigations, are covered through forthcoming chapters, contributing to the overall understanding and characterization of pipe steels.

3 Prediction of Fracture Parameters

3.1 Introduction

While conducting physical tests on specimens or even entire pipes of a specific steel grade remains the gold standard for measuring desired fracture parameters, the cost associated with such endeavors presents a strong barrier. This challenge has led to the emergence of numerical approaches like finite element-based methods (FEM), which offer a means to overcome this limitation. FEM enables researchers to design and simulate numerous models bypassing the constraints of physical testing and facilitating extensive investigations [39].

The finite element method (FEM) serves as an economical and reliable numerical approach to analyze the behavior of pipelines subjected to diverse loading scenarios [40]. Its capacity to offer profound insights into the structural response and operational aspects of pipelines makes it a crucial asset for professionals and researchers within the oil and gas industry. FEM can handle complex shapes and big problems, making it an operational tool for investigating pipeline behavior and solving design and integrity issues. Within the domain of FEM-based techniques, the cohesive zone model (CZM) holds a prominent position as a numerical tool for investigating the dynamics of crack propagation. The foundational work of Barenblatt [41] and Dugdale [42] marked the inception of CZM, illuminating nonlinear behaviors close to crack tips in materials with distinct properties. Building upon this, Hillerborg et al. [43] pioneered the integration of CZM into the FEM framework, with a focus on brittle fracture phenomena in concrete structures.

Extended Finite Element Method (XFEM)-based Cohesive Zone Model (CZM) has recently found more application in fracture modeling. XFEM, goes beyond the traditional finite element analysis, providing advanced capabilities to accurately simulate crack initiation and propagation along arbitrary paths within a given model. The significant advantage of XFEM

lies in its ability to handle crack growth without requiring time-consuming remeshing of the model, making it a highly efficient and practical tool for studying complex fracture behaviors in various engineering structures [44, 7]. Considering the traction separation law (TSL), the objective of the model is to efficiently identify potential regions of crack initiation, based on the stress/strain state at the crack tip and the user-defined damage criteria.

Extended finite element method (XFEM) is an advanced version of the regular finite element method, using damage parameters as material properties input into the model. Damage initiation criteria in XFEM include maximum principal stress (Maxps) or maximum principal strain (Maxpe), with supported damage evolution criteria such as fracture energy (Gc). In XFEM models, damage initiates (or propagation of cracks ensue) when strain, stress, fracture energy, or displacements exceed the specified damage parameters. Various researchers have employed this method, like Zhang et al. [45], who applied it to small-scale X65 steel specimens using Maxps and Gc. Other studies on higher grades of steel, such as X80 by Nonn and Kalwa [46], and X100 by Scheider et al. [47], can also be found. Ameli et al. [48] validated experimental results for X42 steel SENT specimens with XFEM using Maxps and Gc. Lin et al. [19] extended this to a full X52 steel pipe for model validation using experimental results. On the other hand, Okodi et al. [49, 50] utilized Maxpe and Gc to evaluate burst pressure of X60 and X70 pipeline steel with dent crack defects. Liu et al. [51] studied critical crack tip opening displacement in X80 steel pipes using XFEM with the same parameters and Elyasi et al. [40] predicted tensile strain capacity in a full X52 pipe steel body using Maxpe and Gc. Existing literature mainly focuses on X60 and higher-grade steel, motivating us to deeply investigate Vintage X52 pipe steel by conducting various experimental tests on SENT

specimens, and then comparing them with simulated XFEM models using Maxpe and Gc fracture parameters.

The primary emphasis is on a numerical investigation involving three distinct models with varying initial notch sizes, along with the assessment of fracture parameter selection and mesh analysis. Ultimately, the results are compared with corresponding experimental outcomes, assessing the precision and reliability of the chosen fracture parameters.

3.2 Numerical Analysis

3.2.1 XFEM-Based Model Approach

XFEM built-in algorithm within the software ABAQUS employs a technique involving phantom nodes and their superposed original real nodes. As the crack propagates, these nodes gradually separate from each other, strictly adhering to a user-defined TSL and evolution criterion. This approach enables ABAQUS to simulate and monitor crack growth effectively, making it an invaluable tool in the study of fracture mechanics and structural integrity assessments. [49].

3.2.2   XFEM Model Set-Up

In this chapter, three XFEM models as employed within the software ABAQUS based on different SENT geometries are developed, each having different initial notch sizes of $a_0/W=0.2$, $a_0/W=0.3$, and $a_0/W=0.5$. The purpose is to validate these models with the experimental results obtained from specimens having exactly the same notch sizes through various results. The XFEM models are created using the deformable solid extrusion type, and their dimensions precisely matches those of the manufactured and tested specimens, as shown in Figure 3.1.

To ensure accurate interaction between the crack and its surrounding region, from the "interaction" module / "special" icon in the software a new crack created, encompassing the entire area containing the notch edges and crack tip, along with other faces of the specimen. The top and bottom cells of the specimen, which were held by the grips during the experimental test, are coupled to reference points located at the middle of each part. To be more precise, the reference points are located in the upper and lower holes of the specimen and the holes are tied to the reference point using kinematic coupling. This coupling simulates similar restrictive conditions to the experimental setup.

Regarding the boundary conditions, the top part of the specimen is immobilized in all directions, ensuring it remains fixed during the analysis. In contrast, the bottom part is granted full freedom of movement in the vertical direction, with U2 not being restricted in the vertical direction. This setup closely mirrors the boundary condition observed in the actual experimental test. Furthermore, the loading conditions by applying a vertical downward displacement of U2 = 0.1 to the bottom grip is simulated. The 8-node linear brick, reduced integration (C3D8R) element is employed for the entire model. The meshing techniques used are Sweep/Medial axis in the crack growth area, Sweep/Advancing front in the partitioned area close to the crack, and structured mesh in the daylight region. Several researchers, including Lin et al. [39], Elyasi et al. [40], and Afzalimir et al. [21], have conducted mesh convergence analyses in their respective publications. Building on their findings, in the current study a similar strategy has been adopted to achieve computational efficiency, minimize analysis time, and reduce computational effort in the XFEM simulations. By fine-tuning the element sizes within a specific range, from 0.2 mm to 0.5 mm in the crack growth path and 0.5 mm to 2 mm in the daylight and end edges, an optimal balance between accuracy and

computational resources has been ensured, enabling models to obtain reliable results in an efficient manner. Figure 3.2 provides an example of a meshed model with an initial notch size of a_0/W=0.2, illustrating the implementation of the specified element sizes based on the described approach. The utilization of these XFEM models, incorporating precise geometries and boundary conditions, is expected to yield greater insights into fracture behavior and enhance the reliability of the predictions compared to the experimental results.

3.2.3   Material Properties

The elasto-plastic isotropic hardening material model is utilized to simulate the SENT specimen. In order to determine the material properties of X52 pipe steel, a series of five dog bone shape longitudinal specimens were designed, manufactured, and subjected to testing following the ASTM E8/ E8M – 11 [27] in the experimental testing section of the research (chapter 2). The average results obtained from these tests revealed the following material properties for X52 steel: yield stress (σ_{ys}) of 420 MPa, ultimate tensile stress (σ_{uts}) of 607.5 MPa, Young's modulus of 192.5 GPa, and Poisson's ratio of 0.3. These values, along with the plastic characteristics of the steel, were used as material property inputs for the XFEM model. According to the Figure 2.8 in the previous chapter, the average true stress-strain curve employed in the numerical evaluation. Regarding the damage initiation and evolution parameters, Maxpe, fracture energy (Gc) and damage stabilization cohesive (DSC) are initially estimated and used to obtain the most reliable predictions, which are then validated against several experimental results.
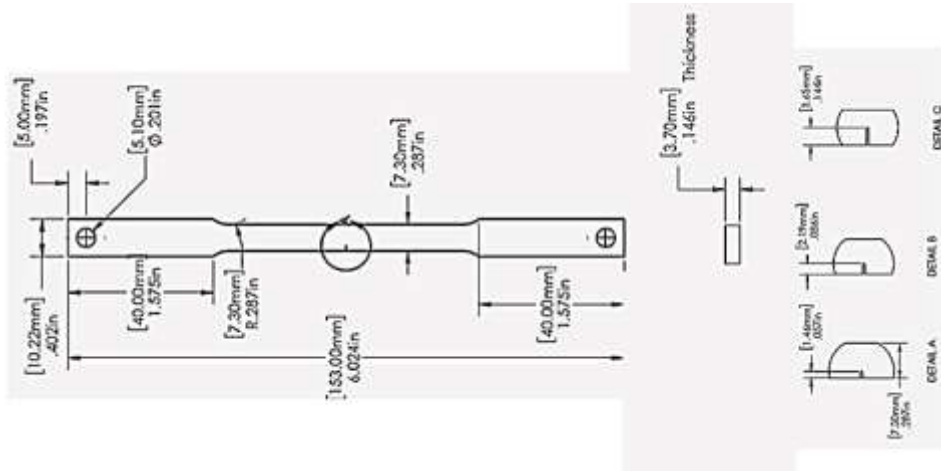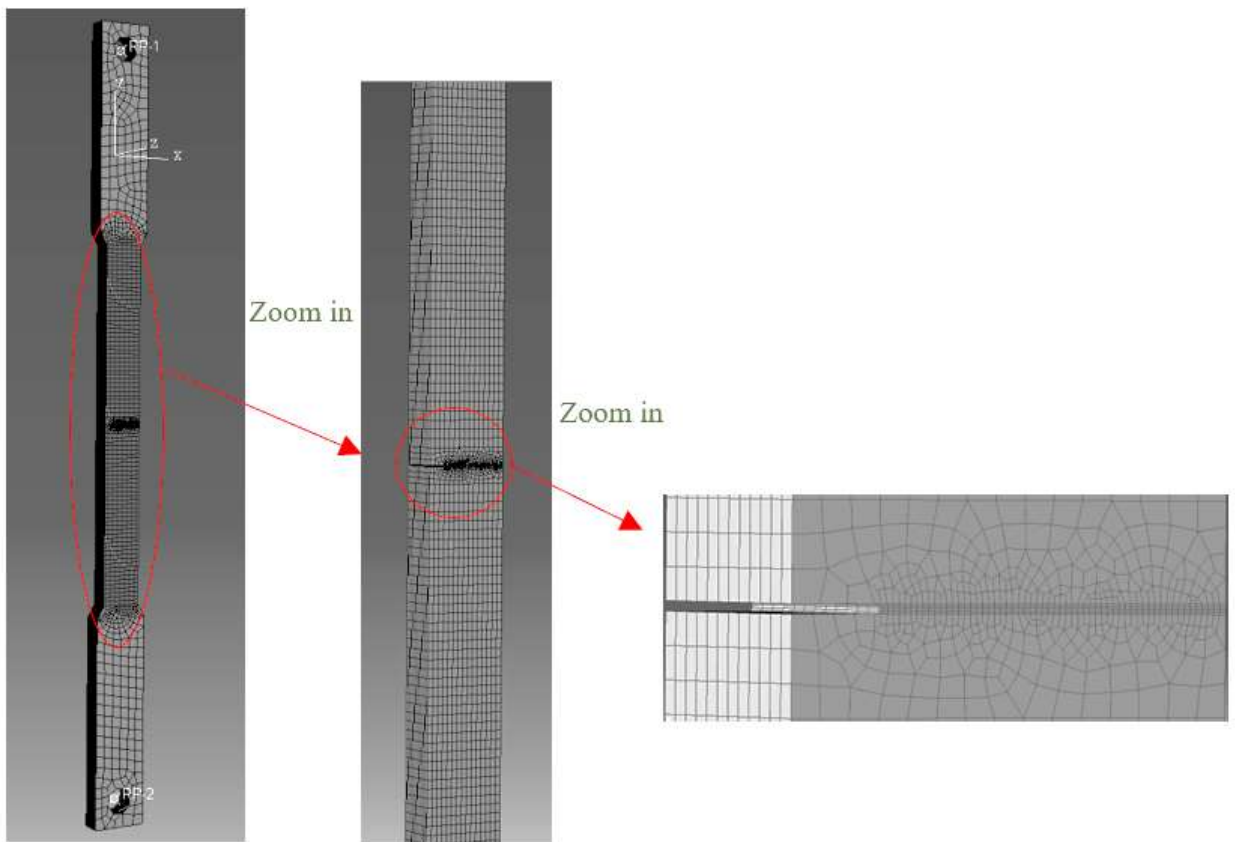
Figure 3.1 Dimensions details of the SENT geometries

Figure 3.2 Meshed model with an initial notch size of a_0/W=0.2

3.3   Results and Discussion

3.3.1 Model Validation

Two damage parameters are obtained through a calibration process, utilizing a method similar to the method used by Elyasi et al. [40] on the XFEM model of vintage X52 Pipe steel. Initially, damage sets are obtained independently for each model, accurately predicting the results of the three experiments. Subsequently, the proper range of Maxpe, Gc and DSC is determined for all models, and the final set of parameters that can predict the results is obtained. The proposed fracture properties for the SENT models are Maxpe = 0.016 mm/mm, Gc = 150 N/mm and $DSC = 10^{-5}$ N/m^2 ($DSC = 10^{-5}$N/m^2 would be kept as a constant value throughout the study). All three models demonstrate minimal calibration errors when fitting the average maximum load and displacement parameters. In the resembling studies focusing on two different X52 vintage pipe by Zhang et al. [52] and Elyasi et al. [40], X42 vintage pipe by Agbo et al. [44], and X60 by Okodi et al. [49] similar parameters were obtained, but with different valuesmethods were used to find the XFEM ideal parameters.

In Zhang's investigation, the parameters for the X52 vintage pipe were determined as Maxpe = 0.020 mm/mm and Gc = 150 N/mm in a full-scale study. In contrast, Elyasi's study reported different values, Maxpe = 0.085 mm/mm and Gc = 900 N/mm, for another full-scale simulation involving different X52 vintage pipes. Transitioning to the X42 vintage pipe, the parameters were identified as Maxpe = 0.013 mm/mm and Gc = 450 N/mm in models representing the full-scale pipe by Agbo. Additionally, in Okodi's research, SENT specimens from the X60 vintage pipe exhibited Maxpe = 0.034 mm/mm and Gc = 150 N/mm.

The noticeable discrepancy between the results from Zhang's and Elyasi's research can be attributed to various factors. An essential factor contributing to the difference, particularly in

the same steel grade (vintage X52), is that the pipes were not sourced from the same lines. These pipes had distinct characteristics, including different *WT*, *OD*, and lengths in the model. Zhang's models were designed with lengths that ensured the applied boundary conditions did not influence the failure pressures, whereas Elyasi's pipes were limited to lengths of 1.2 m and 1.8 m, focusing on calibrating smaller sets of the full pipe body.

Another significant factor is the varied methods employed by Zhang and Elyasi to simulate crack tip and crack opening initiation. Elyasi adopted Lin et al.'s method [39], modeling the crack as a shell planar part positioned in the middle length of the solid part. In contrast, Zhang simulated the crack as a V-notch-shaped crack, similar to the method used by Okodi in his study and the one applied here. Furthermore, Elyasi's pipes were subjected to a combination of internal pressure and external eccentric tension, while Zhang's pipes were simulated under the effect of internal pressure only [52, 40, 49].

The validation process involves a comparison between the numerical predictions and the corresponding experimental Force-CTOD curves, Force-CMOD curves, and Force-Global Displacement curves for all three notch sizes which the global vertical displacement of the specimen, measured from the reference point RF2 located at the bottom part of the specimen (as depicted in Figure 3.2).

3.3.2 Force-CTOD Curves

Figure 3.3 presents a comprehensive comparison of applied tension load-CTOD curves derived from nine experimental tests conducted on three different crack sizes, along with the corresponding XFEM results utilizing Maxpe = 0.016 mm/mm, Gc = 150 N/mm and *DSC* = 10^{-5} N/m^2 as the damage parameters. The findings demonstrate remarkable agreements between the experimental and XFEM results across various regions of the curve,

encompassing the elastic range, maximum load, and energy absorption phase for each crack size. The maximum applied tension load exhibits minimal differences between the experimental and XFEM results, with discrepancies of less than 4% for all specimens with different crack sizes. The largest difference is observed in the $a_0/W = 0.5$ curves, where the XFEM result records 7230 N and the lowest value among the three experimental tests is 6947 N, indicating a difference of 4% in this context.

Regarding the CTOD values at the maximum load points, the corresponding XFEM results vary between 41% higher and 7% lower compared to the experimental results for the three different initial notch sizes. The relatively high percentage difference in CTOD values can be attributed to the scale of CTOD measurements, which is less than a millimeter. Even slight displacements can lead to significant percentage variations. For instance, in the $a_0/W = 0.5$ curves, the XFEM results indicate the maximum load occurs at CTOD = 0.135, while an experimental test shows a CTOD of 0.111 mm at maximum load. These values result in a difference of more than 21%, despite the XFEM result being only 0.024 mm further than the corresponding experimental result.

3.3.3   Force-CMOD Curves

A comparable analysis is conducted for the applied load-CMOD results, and similar to the preceding section, the findings reveal strong concordance between the outcomes from the experimental tests and XFEM analysis. Illustrated in Figure 3.4, it is evident that the XFEM results align closely with the corresponding experimental curves. Notably, the $a_0/W = 0.5$ curve demonstrates the closest resemblance between XFEM and experimental CMOD values. The difference between the CMOD at the point of maximum load for this curve and the farthest experimental CMOD is only 12%. The XFEM-based analysis exhibits impressive

concurrence with experimental findings in predicting fracture parameters. However, it's crucial to acknowledge that minor divergences may emerge during crack propagation due to variables like material inhomogeneity and intricate crack interactions. It's noteworthy that within this study, notable deviations in the crack propagation at XFEM models were not observed.

### 3.3.4 Force- Global Displacement Curves

The validation of XFEM models against experimental results also includes the analysis of the applied tensile force versus global displacement curve. Similar to the previous comparisons, the reliability of the models is readily apparent from Figure 3.5. Notably, the elastic portions of these curves indicate that all three models closely adhere to their corresponding experimental curves, signifying accurate replication of the test conditions by the models. Regarding the displacement at maximum load, aside from $a_0/W = 0.2$ which exhibits a 23% difference between XFEM and experimental results, the other two crack sizes show displacement values at maximum load in XFEM results that are nearly equivalent to those observed in experiments, with differences of less than 10%. Collectively, these outcomes across the aforementioned subsections underscore the dependability and precision of the XFEM approach in predicting fracture parameters. This includes situations where small displacements may contribute to relatively higher percentage discrepancies in CTOD values.
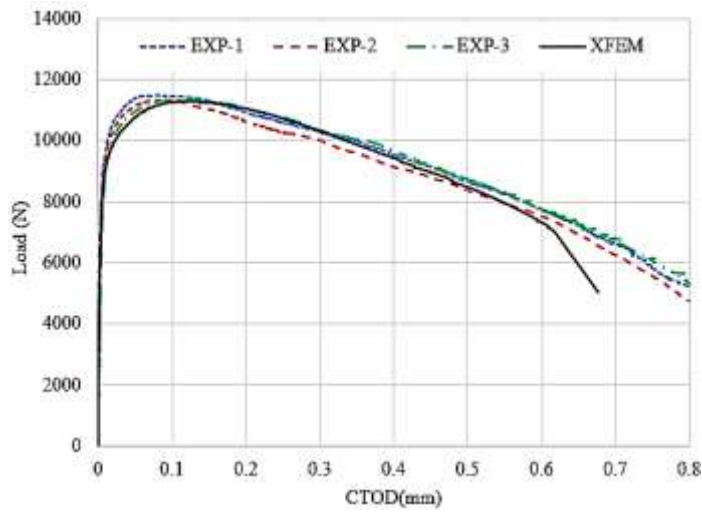
(a) $a_0/W = 0.2$
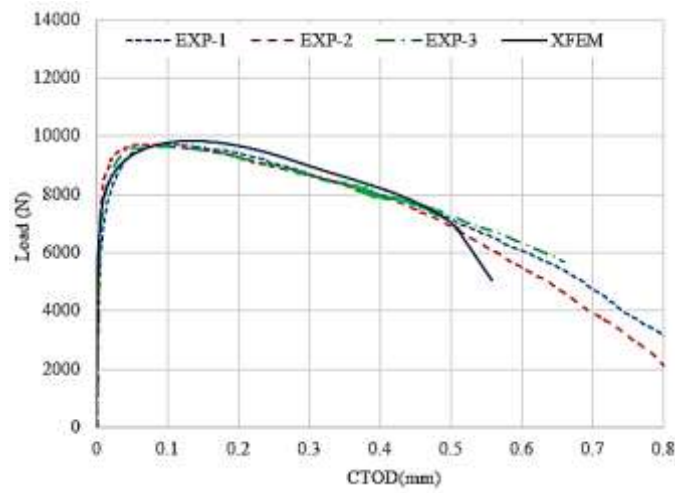
(b) $a_0/W = 0.3$
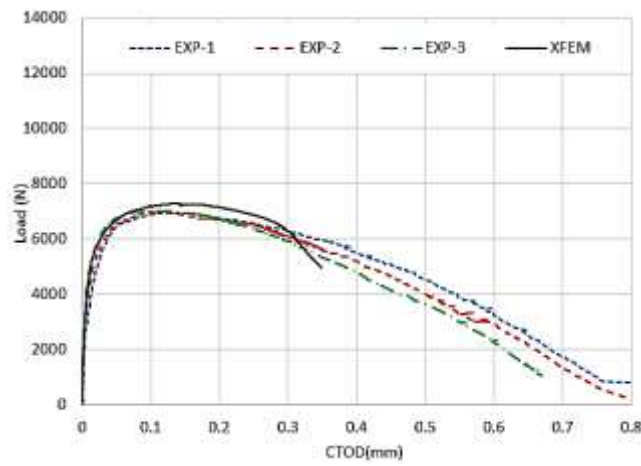
(c) $a_0/W = 0.5$

Figure 3.3 Applied tensile force – CTOD curves (a) a_0/W=0.2 (b) a_0/W=0.3 (c) a_0/W=0.5
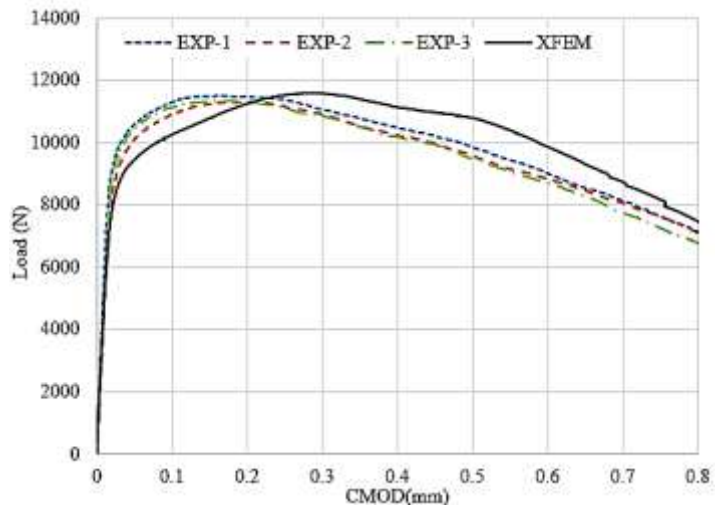
57

(a) $a_0/W = 0.2$
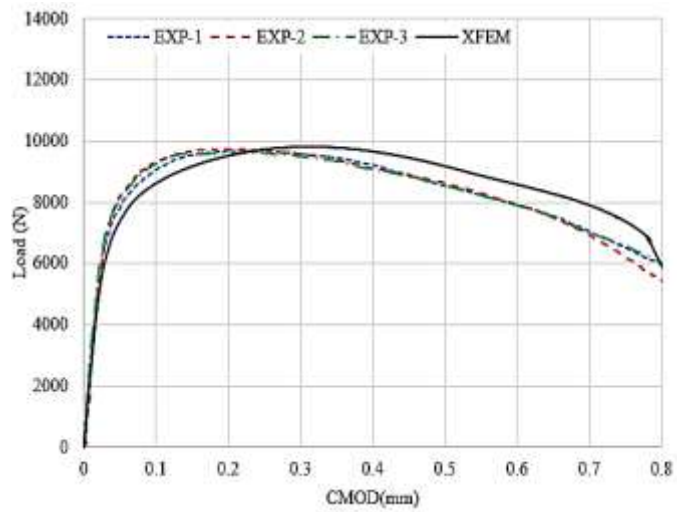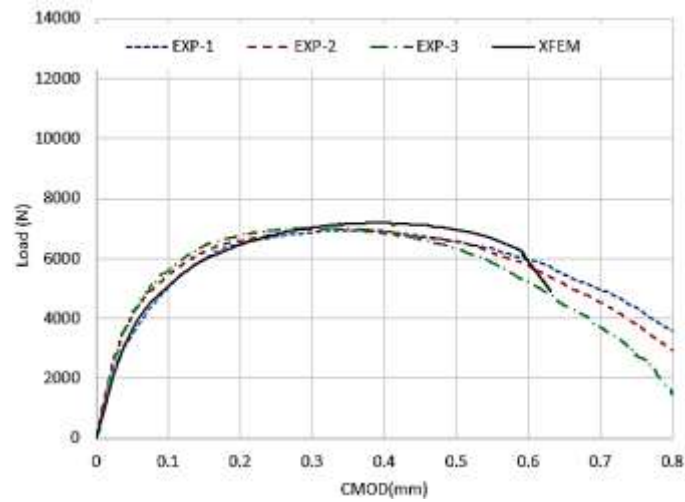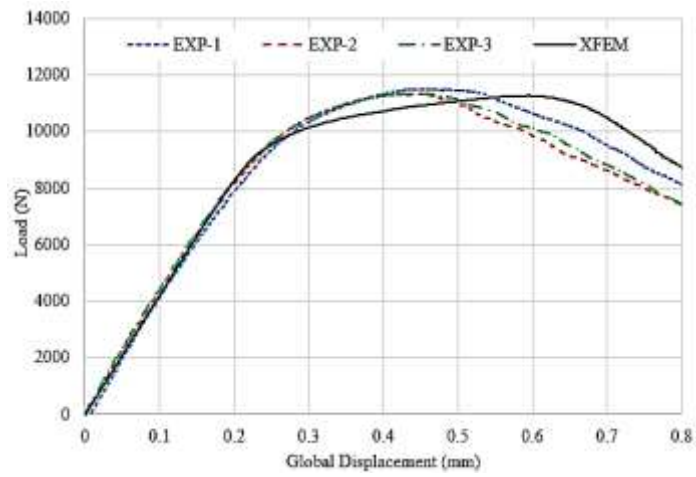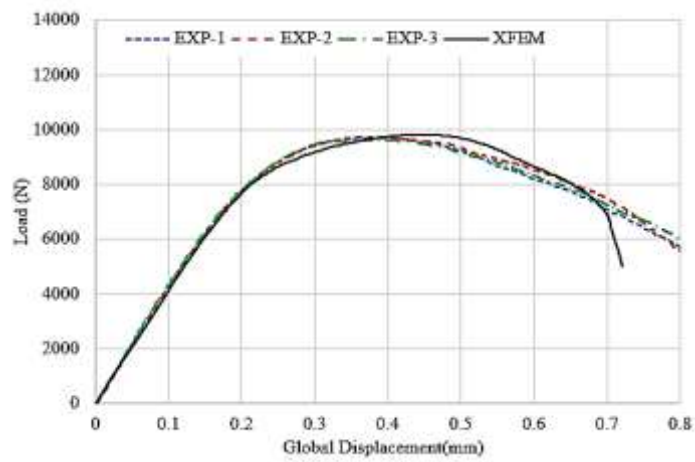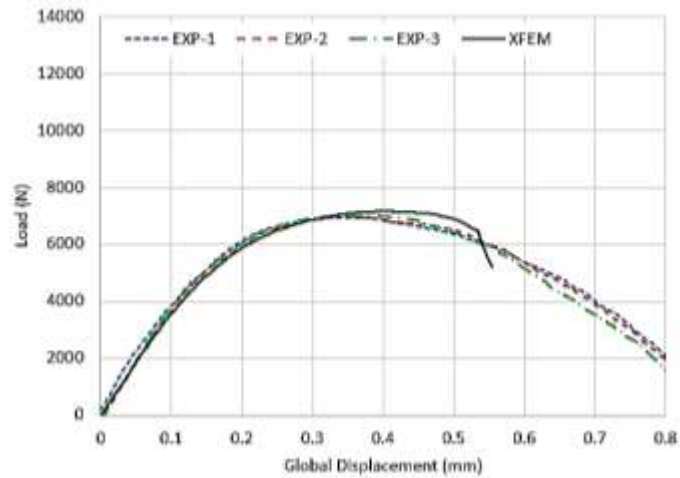

(b) $a_0/W = 0.3$

(c) $a_0/W = 0.5$

Figure 3.4. Applied tensile force – CMOD curves (a) $a_0/W=0.2$ (b) $a_0/W=0.3$ (c) $a_0/W=0.5$

58

(a) a₀/W = 0.2

(b) *a₀/W = 0.3*

(c) a₀/W = 0.5

Figure 3.5. Applied tensile force – Displacement curves (a) a_0/W=0.2 (b) a_0/W=0.3 (c) a_0/W=0.5

3.3.5 Stress triaxiality and ductility

Several studies have explored the relationship between ductile fracture in metals and stress triaxiality at the crack tip. One notable investigation, conducted by Sichani [54], focused on various geometries of X65 pipe steel. Sichani established a variable fracture criterion that correlates ductility with stress triaxiality for X65 pipeline materials. To assess the impact of constraint on fracture, a range of specimens including smooth bar, notched bar, and SENT ($a_0/w = 0.25, 0.5,$ and 0.75) tests were simulated using CZM in XFEM and with fixed value of plastic strain as damage initiation in FEM [54].

Sichani's study revealed a reverse correlation between stress triaxiality at the initiation of the crack and the ductility of SENT specimens with different notch sizes. His findings indicated stress triaxiality values of 0.864, 0.863, and 0.65 for a_0/w ratios of 0.25, 0.5, and 0.75, respectively from FEM models and 1.57, 1.69 and 1.16 from XFEM models. Notably, he observed that an increase in the notch length in SENT specimens resulted in a reduction of stress triaxiality, which was accompanied by an increase in ductility.

In the field of fracture mechanics, the correlation between stress triaxiality and ductility plays a significant role in comprehending material behavior during the initiation of crack formation. Stress triaxiality serves as a vital indicator of crack tip constraints, with higher values signifying elevated constraint levels [55, 56]. Literature indicates that specific stress states align with distinct stress triaxiality values. For example, plane strain conditions are commonly linked with a stress triaxiality of $\eta = \sqrt{3}/3$, reflecting the predominant constraint on the crack tip under such circumstances. Conversely, in scenarios characterized by plane stress, the associated stress triaxiality is typically $\eta = 2/3$ [57, 58]. The association between stress triaxiality and crack tip constraints is thoroughly examined in the works of Donato et al. and

Bai et al. [59, 60], providing insights into the interplay between material deformation and fracture behavior. These studies illustrate that the stress field ahead of the crack tip closely adheres to the high constraint (triaxiality) condition typical of plane-strain.

In the current study, we measured the stress triaxiality at the onset of the crack in SENT models with three different notch sizes (a_0/w = 0.2, 0.3, and 0.5). Figure 3.6 illustrates stress triaxiality versus specimen thickness graphs, each drawn using five data points from the respective model. Th figure indicates that the stress triaxiality values at the middle of the specimen thickness in the cracking area were higher (1.14, 1.08, 1.01, respectively) than at the edges (0.68, 0.64, 0.62, respectively). Furthermore, stress triaxiality exhibited a decrease for specimens with a_0/w = 0.3 and 0.5 in comparison to a_0/w = 0.2, consistent with Sichani's reported trend. This supports the idea of a more ductile condition in specimens with a_0/w = 0.5 than 0.3 and 0.2, respectively, in good agreement with our experimental results.

For the described XFEM models, we used the same damage criterion for all the specimens which, surprisingly, still resulted in different ductility for the different specimens. Given the similar geometry of the SENT specimens used in our paper, the stress triaxiality values and reported critical CTOD values are very close to each other, with only slight differences attributable to the varied notch sizes. Our future work will focus on developing models where XFEM damage criterion are function of the stress triaxiality as described by Lin et.al. [61].
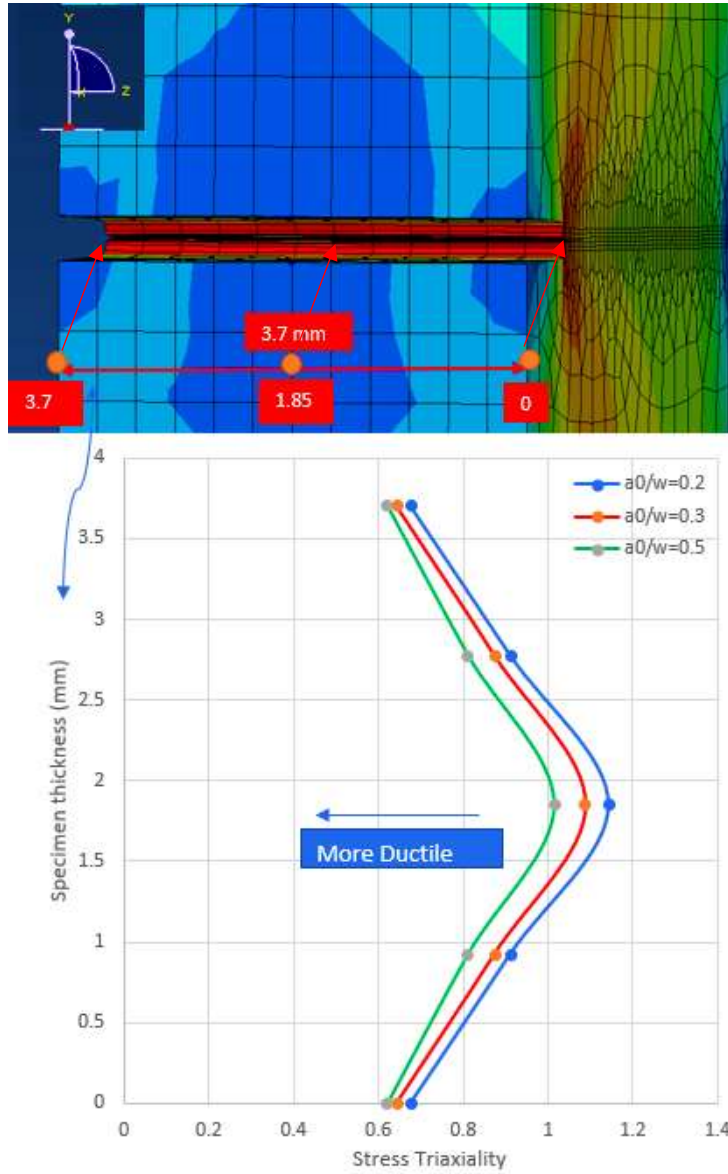
Figure 3.6. Specimen thickness vs stress triaxiality

3.3.6 Mesh Analysis

To assess the mesh dependency of the designed XFEM models, various simulations were conducted using different mesh sizes and types in the proximity of the crack path. This meticulous mesh analysis aimed to scrutinize the influence of mesh variations on the XFEM model outcomes. The fracture parameters, Maxpe = 0.016 mm/mm and Gc = 150 N/mm, were held constant throughout these simulations to maintain consistency.

The range of mesh sizes adjacent to the crack tip along the crack path included 0.1 mm, 0.2 mm, and 0.5 mm, representing medial axis, structured, and advancing front mesh types, respectively (as illustrated in Figure 3.7). This diverse set of simulations ensures a comprehensive exploration of the XFEM model's behavior under different mesh conditions.

In Figure 3.8, the applied tensile load–CTOD curves of three XFEM models for SENT specimens with a0/W=0.2 are depicted, utilizing the aforementioned meshes. A comparative analysis with experimental test results highlights a substantial alignment between the XFEM model predictions and the empirical data, affirming the robustness of the XFEM approach. Even when the mesh size in the crack area increases approximately fivefold, the results remain within an accurate range. Minor discrepancies, primarily observable in the energy absorption segment, are minimal and do not compromise the overall accuracy and reliability of the XFEM models. This comprehensive mesh analysis reinforces the credibility of the XFEM approach and its consistent performance across diverse mesh conditions.
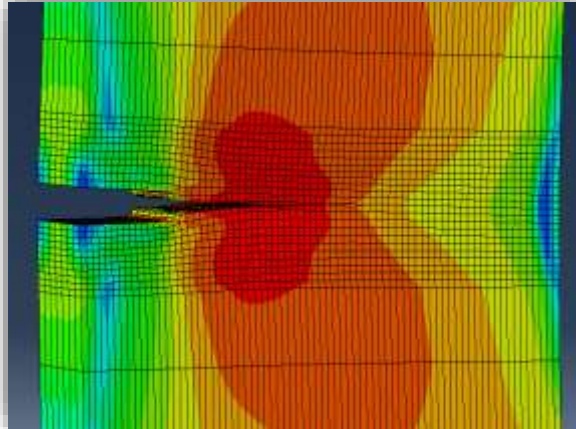
(a)
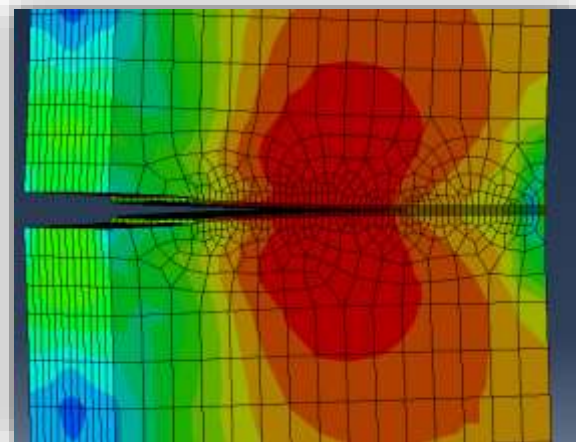
(b)
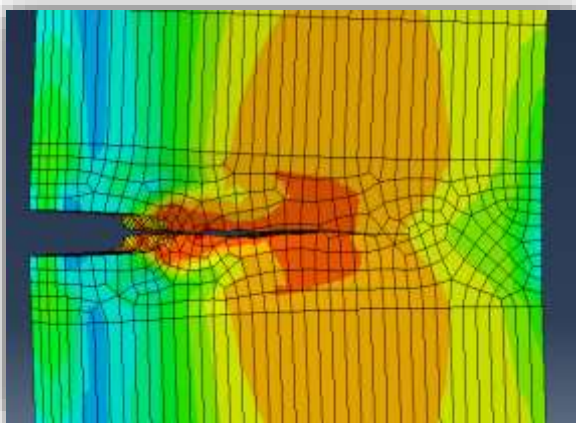
(c)

Figure 3.7 Various mesh type and mesh size near the crack growth path (a) 0.1 mm – Medial Axis
(b) 0.2 mm - Structured (c) 0.5 mm–Advancing front

64
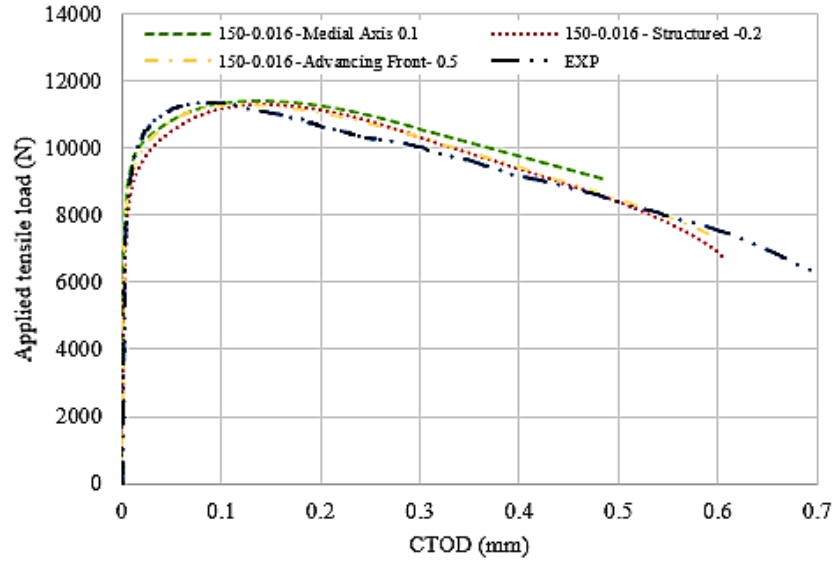
Figure 3.8 Applied tensile force – CTOD curves of three models with different mesh

3.3.7 Comparison of Different Maxpe and Different Fracture Energy

Within this subsection, a comprehensive investigation has been carried out to explore the effects of varying fracture parameters on model outcomes and their alignment with experimental results. Figure 3.9 illustrates the outcomes of three different models for a_0/W=0.2, while keeping Gc = 150 N/mm constant and altering Maxpe values to 0.013, 0.016, and 0.019. The curves notably emphasize the accuracy and alignment achieved with a Maxpe value of 0.016, whereas the other two values exhibit sensible deviations from the experimental results, marked errors.

Furthermore, the curves depicted in Figure 3.10 illustrate a notable gap between experimental outcomes and XFEM simulations when employing different fracture energies (Gc) of 120, 150, and 180 N/mm, while maintaining Maxpe = 0.016 as a constant parameter. Similar conclusions can be drawn from these curves, indicating that 150 N/mm stands as the most suitable value for running the models to effectively replicate the experimental specimens. Figure 3.6 also elucidates that Gc value lower than 150 N/mm leads to faster energy release,

65

potentially impacting the point of maximum load. Conversely, when the Energy exceeds 150

N/mm, the curve ascends to higher levels after reaching the maximum load, resulting in

smoother energy absorption. This distinctive behavior accounts for its prominent placement

at the top of the graph when Gc = 150 N/mm is applied. Comparable findings were observed

in the study conducted by Zhang et al. [52], showcasing the consistent behavior observed
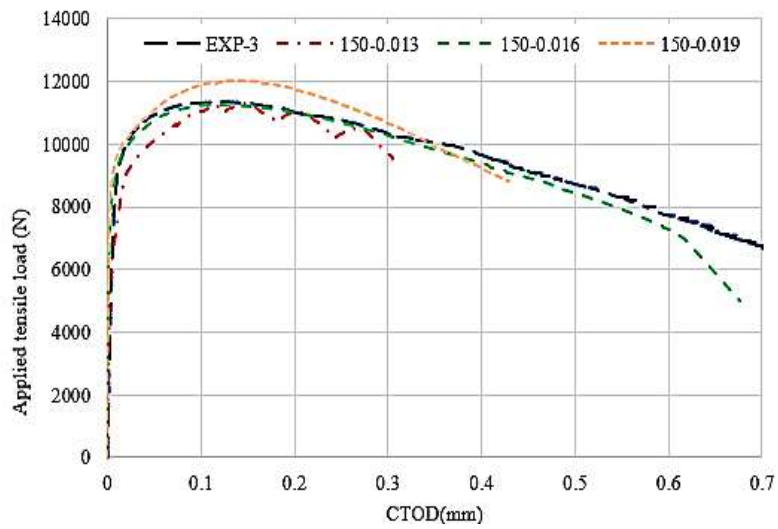
when altering Maxpe and Gc values.

Figure 3.9 Applied tensile force – CTOD curves of three models with different Maxpe
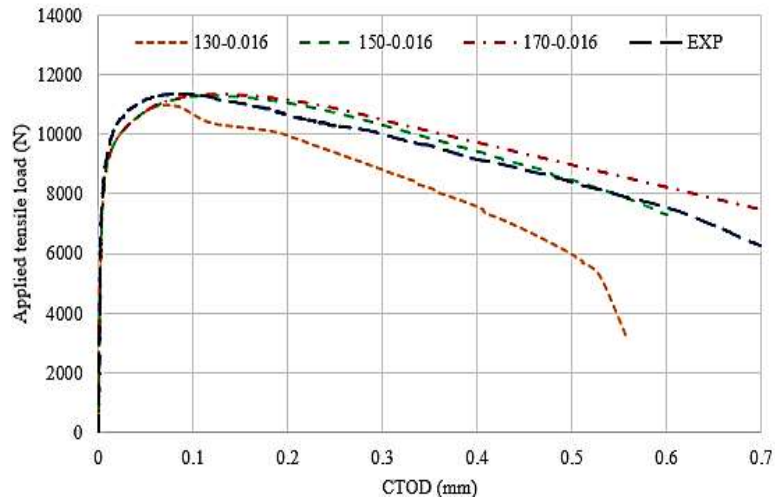

Figure 3.10 Applied tensile force – CTOD curves of three models with different *Gc*

Collectively, the credibility of the XFEM models utilizing Maxpe = 0.016, Gc = 150 N/mm and $DSC = 10^{-5} N/m^2$ as fracture parameters is substantiated across all models with varying notch sizes. Similar research endeavors in the literature reveal a substantial concordance between their XFEM outcomes and experimental results. For example, Zhang et al.'s [52] investigation on X52 steel full pipe bodies employing Maxpe = 0.020 and Gc = 150 N/mm demonstrated XFEM models capably predicting tensile strain along the pipe length using the suggested fracture characteristics. In Okodi's study, the SENT specimens derived from the X60 vintage pipe displayed parameters with Maxpe = 0.034 mm/mm and Gc = 150 N/mm [49]. Another study by Liu et al. [51], focusing on SENT specimens derived from X80 steel grade, showcases the closest model-to-experiment alignment with Maxpe = 0.08 and Gc = 200 N/mm.

While stress-based damage initiation employed in studies using Maxps and Gc is reliable as well, it's noteworthy that Ameli's [48] and Lin's [39] simulations reported a maximum principal stress surpassing the material's ultimate stress. This indicates that such a damage criterion might not be practical for modeling materials subject to plastifying crack tips, raising potential concerns.

3.4 Conclusion

In the realm of pipeline steel fracture behavior, this study presents a comprehensive approach that seamlessly integrates experimental testing with numerical analysis using the Extended Finite Element Method (XFEM). The focus on SENT specimens made from Vintage X52 pipe steel adds depth to the understanding of fracture characteristics. The XFEM models, calibrated with fracture parameters Maxpe = 0.016 mm/mm, Gc = 150 N/mm and $DSC = 10^{-5}$ N/m^2, demonstrate great reliability and accuracy in predicting crack initiation and propagation for

various initial notch sizes. The comprehensive analysis of both experimental and numerical outcomes throughout the Force-CTOD, Force-CMOD, and Force-Global Displacement curves highlights the reliability of the selected parameters and the XFEM approach. The findings not only validate the efficacy of XFEM in predicting fracture behavior but also highlight the importance of accurate parameter selection for precise simulation outcomes. This research contributes to advancing the knowledge of pipeline steel fracture mechanics and offers valuable insights for designing and maintaining safe and efficient energy transportation systems.

Further investigations are currently underway by the other researchers in our research group, encompassing additional geometries such as CT and SENB, to expand the insight on the studied steel material. This endeavor aims to compile a comprehensive database of fracture parameters, leading to the recommendation of a unified model. This model will serve as a crucial reference point, enabling the establishment of criteria to correlate experimental fracture parameters with predictive outcomes. Moreover, this research serves as a launching pad for the potential application of the same methodology to diverse steel grades. By doing so, it can mitigate the substantial costs associated with conducting separate evaluations for different pipe materials. Considering insights gained from studies conducted on full-scale pipes of the same steel grade, this study not only successfully bridges the gap between experimental testing and numerical analysis but also enforces the groundwork for more precise predictions of fracture behavior in pipeline materials.

2.2   Discussion

4   Summary, Conclusion, and Future Direction

4.1 Summary

The main objectives and goals of this project were to comprehensively investigate the fracture toughness of API X52 pipeline steel, focusing on small-scale SENT experimental tests and XFEM models. The project aimed to provide valuable insights into the fracture behavior under various conditions and contribute to the understanding of pipeline steel fracture mechanics.

In the first chapter, the significance of fracture toughness and its relevance to pipeline steel, especially in the context of SENT specimens, was highlighted. The methodology involved a multi-specimen strategy, aligning with BS 8571:14 guidelines, to explore the complex relationship between fracture toughness and crack size. This chapter laid the foundation for subsequent experimental and numerical analyses.

Chapter 2 focuses the SENT experimental tests, detailing the setup, methodologies, and results. Noteworthy innovations included the use of strain contours for Δa measurements and the correlation of Force-CTOD and Force-CMOD curves. The comparative analysis of X52 steel with higher grades enriched the understanding of material performance, and the results were presented in Force-CTOD, Force-CMOD, and R-curves.

Chapter 3 introduced XFEM models, emphasizing the use of Maxpe, Gc, and damage stabilization cohesive (DSC) fracture parameters. The numerical analysis involved three models with varying initial notch sizes, validated against experimental results. XFEM set-up, mesh analysis, and material properties were meticulously explained. The findings reinforced the reliability of XFEM in predicting fracture behavior, contributing valuable insights to pipeline steel fracture mechanics.

4.2 Prominent Accomplishments

Innovative Measurement Approach: The project introduced an innovative approach for Δa measurements using strain contours in Vic 3D software, providing a novel way to analyze crack growth.

Comparative Analysis: Comparative analysis of X52 steel with higher grades (X65, X80, X90, X100) enriched the understanding of fracture characteristics, aiding material selection and design decisions.

XFEM fracture variable prediction: The XFEM models, calibrated with specific fracture parameters, demonstrated high reliability and accuracy in predicting crack initiation and propagation, showcasing the effectiveness of numerical analysis.

Insights into Material Properties: The project provided detailed insights into the material properties of X52 steel, crucial for designing and maintaining safe energy transportation systems.

4.3 Future Works

While the summary encapsulates the key achievements of the project, future works may focus on:

Expanded Geometries: Conducting additional tests on different geometries such as CT and SENB to broaden the database of fracture parameters and establish a unified model.

Application to Diverse Steel Grades: Extending the methodology to diverse steel grades to create a more versatile and cost-effective approach applicable across various pipeline materials.

Correlation Criteria: Establishing criteria to correlate experimental fracture parameters with predictive outcomes, facilitating more precise predictions of fracture behavior.

Full-Scale Pipe Studies: Building on insights gained from studies on full-scale pipes of the same steel grade, further investigations could bridge the gap between experimental testing and numerical analysis.

Establishing precise criteria to correlate experimental fracture parameters with predictive outcomes is crucial for more accurate predictions of fracture behavior.

References

[1] *API Specification 5L: Specification for Line Pipe. 45th Edition, December 2012.*

[2] *Title: Creep, Website: Iowa State University Center for Nondestructive Evaluation, URL: https://www.nde-ed.org/Physics/Materials/Mechanical/Creep.xhtml*

[3] *Bhushan, B. (2013). Principles and applications of tribology (2nd ed.). New York, NY: Wiley.*

[4] *Anderson, T. L. (2005). Fracture mechanics: fundamentals and applications (3rd ed). Boca Raton, FL: Taylor & Francis Group.*

[5] *Drexler, E., Wang, Y.-Y., Sowards, J. W., & Dvorak, M. D. (2010). SE(T) Testing of Pipeline Welds. Proceedings of the 2010 8th International Pipeline Conference, Vol. 4 (pp. 149-158). New York, NY: American Society of Mechanical Engineers (ASME). doi:10.1115/IPC2010-31325*

[6] *Verstraete, M., Hertele, S., Waele, W. D., Denys, R., & Minnebruggen, K. V. (2012). Measurement of ductile crack extension in single edge notch tensile specimens. Proceedings of 15th International Conference on Experimental Mechanics (ICEM 15). Retrieved from.*

[7] *Zhang, Z., Xu, J., Nyhus, B., & Østby, E. (2010). SENT (Single edge notch tension) methodology for pipeline applications. Proceeding of the 18th European Conference on Fracture, Vol 18 (pp.1-8).*

[8] *BS 8571-14:2014. "Fracture mechanics toughness tests. Method for testing metallic materials using SENT specimens." British Standards Institution, London.*

[9] *M. Chiesa, B. Nyhus, B. Skallerud, C. Thaulow, Efficient fracture assessment of pipelines. A constraint-corrected SENT specimen approach, Engineering Fracture Mechanics 68(5) (2001) 527-547.*

[10] *Kudari, S., B. Maiti, and K. Ray, The effect of specimen geometry on plastic zone size: a study using the J integral. The Journal of Strain Analysis for Engineering Design, 2007. 42(3): p. 125-136.*

[11] *Canadian Energy Pipeline Association, Transmission Pipeline Industry Performance Report, 2018.*

[12] *Yang T, Chen X, Fan Z. A comparison of fracture assessment methods in several structural integrity assessment procedures. In: Proc. ASME PVP Conf., Prague, Czech, July 26e30; 2009. DOI:10.1115/PVP2009-77609*

[13] *Rice JR. A path independent integral and the approximate analysis of strain concentrations by notches and cracks. J. Appl. Mech. 1968;35:379e86. DOI:10.1115/1.3601206*

[14] *Wells AA. Application of fracture mechanics at and beyond general yielding. Br. Weld. J. 1963;10:563e70.   DSIR 23/31374*

[15] *ISO, Metallic materials – method of constraint loss correction of CTOD fracture toughness for fracture assessment of steel components, (2009).*

[16] *American Petroleum Institute, API 1104: welding of pipelines and related facilities, (2010)*

[17] *W. Cheng, H. Tang, P.C. Gioielli, K. Minnaar, M.L. Macia, Test methods for characterization of strain capacity—comparison of R-curves from SENT/CWP/FS tests, (2009) Presented at 5th Pipeline Tech Conf., Ostend, Belgium. 1572824500831200512*

[18] *Weeks, T. S., & Read, D. T. (2015). Comparison of J-integral from single specimen SE(T) tests on API-5L X100 line pipe steel. In ISOPE 2015 Conference (pp. 1-6). Kona, HI.*

[19] *Pussegoda, L. N., Tiku, S., Park, D., Tyson, W. R., & Gianetto, J. (2012). J-Resistance Results From Multi-Specimen and Single-Specimen Surface Notched SEN(T) Geometry. In Proceedings of the 2012 9th International Pipeline Conference (Vol. 3: Materials and Joining, pp. 539-544). Calgary, Alberta, Canada: ASME. doi:10.1115/IPC2012-90565*

[20] *Kong, L., Zhou, X., Chen, L. et al. Experimental Study on the Fracture Toughness of Welded Joints of API X90 High-grade Pipeline Steels Using Single-Edge-Notched Tension Specimens. Arab J Sci Eng **44**, 1033–1041 (2019). https://doi.org/10.1007/s13369-018-3396-7.*

[21] *Afzalimir, S. H., Barbosa, V. S., & Ruggieri, C. (2020). Evaluation of CTOD resistance curves in clamped SE(T) specimens with weld centerline cracks. Engineering Fracture Mechanics, 240, 107326. ISSN 0013-7944.*

[22] *API. (2020). API 5L Pipe Specification (46th Edition, Updated on 2020). American Petroleum Institute.*

[23] *Det Norske Veritas. (2006). DNV-RP-F108: Recommended Practice - Fracture Control for Pipeline Installation Methods Introducing Cyclic Plastic Strain.*

[24] *CanmetMATERIALS. (2012). Recommended Practice: Fracture Toughness Testing Using SE(T) Samples with Fixed Grip Loading. CANMET Materials Technology Laboratory, Natural Resources Canada.*

[25] *ExxonMobil Upstream Research Company. (2010). Measurement of Crack Tip Opening Displacement (CTOD) - Fracture Resistance Curves Using Single-Edge Notched Tension (SENT) Specimens.*

[26] *M.A. Verstraete, R.M. Denys, K. Van Minnebruggen, S. Hertelé, W. De Waele (2013). "Determination of CTOD resistance curves in side-grooved Single-Edge Notched Tensile specimens using full field deformation measurements." Engineering Fracture Mechanics, 110, 12-22. ISSN 0013-7944.*

[27] *ASTM E8/E8M-11, Standard Test Methods for Tension Testing of Metallic Materials, ASTM International, West Conshohocken, PA, 2011*

[28] *E. Fagerholt, E. Østby, T. Børvik, O.S. Hoppersta, Investigation of fracture in small scale SENT tests of a welded X80 pipeline steel using Digital Image Correlation with node splitting, Eng Fract Mech 96 (2012) 276–293. 10.1016/j.engfracmech.2012.08.007*

[29] *Correlated Solutions Inc. 2012. <http://www.correlatedsolutions.com>.*

[30] *Bigger, R., Blaysat, B., Boo, C., Grewer, M., Hu, J., Jones, A., Klein, M., Lava, P., Pankow, M., Raghavan, K., Reu, P. L., Schmidt, T., Siebert, T., Simonsen, M., Trim, A., Turner, D. Z., Vieira, A., & Weikert, T. (2018). A Good Practices Guide for Digital Image Correlation.*

[31] *Tu, S.; Ren, X.; He, J.; Zhang, Z. Stress–strain curves of metallic materials and post-necking strain hardening characterization: A review. Fatigue Fract. Eng. Mater. Struct. 2020, 43, 3–19.02:05 AM*

[32] *H. Tang, M. Macia, K. Minnaar, P. Gioielli, S. Kibey, D. Fairchild, Development of the SENT test for strain based design of welded pipelines, Proceedings IPC 2010 8th international pipeline conference, calgary, Canada, 2010 September 27 to October 1.*

[33] *Iman Ameli, Behrouz Asgarian, Meng Lin, Sylvester Agbo, Ali Imanpour, Da-Ming Duan, Roger Cheng, Samer Adeeb, Determination of CMOD-force curves and R-curves in side-grooved single edge notched tensile (SENT) specimens in welded X42 pipeline steel, International Journal of Pressure Vessels and Piping, Volume 163, 2018, Pages 68-74, ISSN 0308-0161, https://doi.org/10.1016/j.ijpvp.2018.04.003.*

[34] *ISO 12135, Metallic materials – unified method of test for the determination of quasistatic fracture toughness, (2016).*

[35] *Tyson, W.R. and Gianetto, J.A., 2013, Low-Constraint Toughness Testing: Results of a Round Robin on a Draft SE(T) Test Procedure," Proceedings of the ASME Pressure Vessels & Piping Division Conference (PVP2013), Paris, France, Paper PVP2013-97299.*

[36] *K.H. Schwalbe, J. Heerens, U. Zerbst, H.G. Pisarski, M. Koçak, EFAM GTP 02: the GKSS test procedure for determining the fracture behavior of materials, (2002).*

[37] *Park, D.-Y., Gravel, J.-P., Simha, C. H. M., & Liang, J. (September 2014). Fracture Toughness of X70 Pipe Girth Welds Using Clamped SE(T) and SE(B) Single-Specimens. In Proceedings of the International Pipeline Conference (IPC2014-33233) (pp. 1-8). DOI: 10.1115/IPC2014-33233.*

[38] *Sarzosa, D. F. B., Savioli, R., Ruggieri, C., & Garmbis, A. G. (August 2020). Comparison of Fracture Toughness Curves Obtained by Single and Multi-Specimen Methodologies for a Pipe Having an Undermatched Girth Weld. In ASME 2020 Pressure Vessels & Piping Conference, Proceedings of the ASME Pressure Vessels and Piping Division (PVP2020-21546) (pp. 1-8). DOI: 10.1115/PVP2020-21546.*

[39] *Lin, M.; Agbo, S.; Duan, D.-M.; Cheng, J.J.R.; Adeeb, S. Simulation of Crack Propagation in API 5L X52 Pressurized Pipes Using XFEM-Based Cohesive Segment Approach. J. Pipeline Syst. Eng. Pract. 2020, 11, 04020009.*

[40] *Elyasi, N.; Shahzamanian, M.; Lin, M.; Westover, L.; Li, Y.; Kainat, M.; Yoosef-Ghodsi, N.; Adeeb, S. Prediction of Tensile Strain Capacity for X52 Steel Pipeline Materials Using the Extended Finite Element Method. Appl. Mech. 2021, 2, 209-225. https://doi.org/10.3390/applmech2020013*

[41] *Barenblatt, G. I. 1959. "The formation of equilibrium cracks during brittle fracture. General ideas and hypotheses. Axially-symmetric cracks." J. Appl. Math. Mech. 23 (3): 622–636. https://doi.org/10.1016/0021 -8928(59)90157-1.*

[42] *Dugdale, D. S. 1960. "Yielding of steel sheets containing slits." J. Mech. Phys. Solids 8 (2): 100–104. https://doi.org/10.1016/0022-5096(60) 90013-2.*

[43] *Hillerborg, A., M. Modéer, and P.-E. Petersson. 1976. "Analysis of crack formation and crack growth in concrete by means of fracture mechanics and finite elements." Cem. Concr. Res. 6 (6): 773–781. https://doi.org /10.1016/0008-8846(76)90007-7.*

[44] *Agbo, S.; Lin, M.; Ameli, I.; Imanpour, A.; Duan, D.M.; Cheng, J.J.R.; Adeeb, S. Evaluation of the Effect of Internal Pressure and Flaw Size on the Tensile Strain Capacity of X42 Vintage Pipeline Using Damage Plasticity Model in Extended Finite Element Method. In Proceedings of the American Society of Mechanical Engineers, Pressure Vessels and Piping Division (Publication) PVP, San Antonio, TX, USA, 14–19 July 2019; American Society of Mechanical Engineers (ASME): San Antonio, TX, USA, 2019; Volume 5, p. PVP2019-94005*

[45] *Zhang, Bojun, et al. "Ductile failure analysis and crack behavior of X65 buried pipes using extended finite element method." Engineering Failure Analysis 45 (2014): 26-40.*

[46] *Nonn, A., and C. Kalwa. 2013. "Analysis of dynamic ductile fracture propagation in pipeline steels: A damage-mechanics' approach." In Proc., 6th Int. Pipeline Technology Conf. Duisburg, Germany: European Pipeline Research Group.*

[47] *Scheider, I., A. Nonn, A. Völling, A. Mondry, and C. Kalwa. 2014. "A damage mechanics based evaluation of dynamic fracture resistance in gas pipelines." Procedia Mater. Sci. 3: 1956–1964. https://doi.org/10.1016/j.mspro.2014.06.315.*

[48] *Ameli, I., Asgarian, B., Lin, M., Agbo, S., Cheng, R., Duan, D., Adeeb, S., "Estimation of the CTOD-crack growth curves in SENT specimens using the eXtended finite element method," International Journal of Pressure Vessels and Piping, Volume 169, 2019, Pages 16-25, ISSN 0308-0161, https://doi.org/10.1016/j.ijpvp.2018.11.008.*

[49] *Okodi, A.; Lin, M.; Yoosef-Ghodsi, N.; Kainat, M.; Hassanien, S.; Adeeb, S. Crack Propagation and Burst Pressure of LongitudinallyCracked Pipelines Using Extended Finite Element Method. Int. J. Press. Vessel. Pip. 2020, 184, 104115*

[50] *Okodi, A.; Li, Y.; Cheng, R.; Kainat, M.; Yoosef-Ghodsi, N.; Adeeb, S. Crack Propagation and Burst Pressure of Pipeline with Restrained and Unrestrained Concentric Dent-Crack Defects Using Extended Finite Element Method. Appl. Sci. 2020, 10, 7554.*

[51] *Liu, B.; Liu, X.J.; Zhang, H. Strain-Based Design Criteria of Pipelines. J. Loss Prev. Process. Ind. 2009, 22, 884–888.*

[52] *Zhang, Xinfang & Lin, Meng & Okodi, Allan & Tan, Leichuan & Leung, Juliana & Adeeb, Samer. (2021). Numerical Analysis of API 5L X42 and X52 Vintage Pipes with Cracks in Corrosion Defects Using Extended Finite Element Method. Journal of Pressure Vessel Technology. 143. 10.1115/1.4050988.*

[53] *Ohata, Mitsuru & Fukahori, Takuya & Minami, Fumiyoshi. (2010). Damage Model for Predicting the Effect of Steel Properties on Ductile Crack Growth Resistance. International Journal of Damage Mechanics - INT J DAMAGE MECH. 19. 441-459. 10.1177/1056789509103704.*

[54] *Sichani, Mohammadmehdi. (2022). A unified fracture model for X65 pipeline material under various constraints using the eXtended finite element method (XFEM). 10.21203/rs.3.rs-2383493/v1.*

[55] *Sun, Jun. (1993). Stress triaxiality constraint and crack tip parameters. Engineering Fracture Mechanics - ENG FRACTURE MECH. 44. 789-806. 10.1016/0013-7944(93)90206-8.*

[56] *Meshii, T. "Crack-Tip Constraint and Fracture Toughness of an Inner-Surface Crack Under Thermal Shock."* Proceedings of the ASME 2012 Pressure Vessels and Piping Conference. Volume 3: Design and Analysis. *Toronto, Ontario, Canada. July 15–19, 2012. pp. 283-287. ASME. https://doi.org/10.1115/PVP2012-78038*

[57] *Ebelsheiser, Heiko, Markus Feucht and Frieder Neukamm. "On Calibrating Advanced Damage Models Using Sheet Metal Coupon Tests." (2008).*

[58] *Isik, Kerim & Soyarslan, Celal & Richter, Helmut & Tekkaya, A.. (2011). Analysis of formability of advanced high strength steel sheets with phenomenologically based failure criteria with separate treatment of instability, shear and normal fracture.*

[59] *Donato, GHB, Hippert, E, Jr., Donato, GVP, & Ruggieri, C. "Constraint Effects and Crack Driving Forces in Surface Cracked Pipes Subjected to Reeling." Proceedings of the ASME 2008 27th International Conference on Offshore Mechanics and Arctic Engineering. Volume 3: Pipeline and Riser Technology; Ocean Space Utilization. Estoril, Portugal. June 15–20, 2008. pp. 333-342. ASME. 10.1115/OMAE2008-57380*

[60] *Bai, Yuanli & Teng, X. & Wierzbicki, Tomasz. (2009). On the Application of Stress Triaxiality Formula for Plane Strain Fracture Testing. Journal of Engineering Materials and Technology-transactions of The Asme - J ENG MATER TECHNOL. 131. 10.1115/1.3078390.*

[61] *Lin, Meng & Li, Yong & Cheng, J.J. & Koduru, Smitha & Kainat, Muntaseer & Zhang, Xinfang & Adeeb, Samer. (2022). Novel XFEM Variable Strain Damage Model for Predicting Fracture in Small-scale SENT and Full-scale Pipe Tests. Engineering Fracture Mechanics. 271. 108628. 10.1016/j.engfracmech.2022.108628.*